

Direct Influences of Mesospheric Gravity Waves on Ionosphere over Jammu & Kashmir, India

Ramkumar Thokuluwa (✉ tkram@narl.gov.in)

National Atmospheric Research Laboratory

Manzoor Malik

University of Kashmir

Bilal Ganaie

University of Kashmir

Aashiq Bhat

University of Kashmir

Article

Keywords: Subtropical Mesospheric Gravity Waves, Medium Scale Travelling Ionospheric Disturbances (MSTIDs)

Posted Date: October 26th, 2020

DOI: <https://doi.org/10.21203/rs.3.rs-84700/v1>

License: © ⓘ This work is licensed under a Creative Commons Attribution 4.0 International License.

[Read Full License](#)

1 **First-Time Airglow-Imager Based Observation of Direct Influences of Subtropical**
2 **Mesospheric Gravity Waves on F-region Ionosphere over Jammu & Kashmir, India**

3
4 T. K. Ramkumar^{1*}, Manzoor Ahmad Malik², Bilal Ahmad Ganaie² and Aashiq Hussain Bhat²

5
6 1. National Atmospheric Research Laboratory, DOS, Govt. of India, Gadanki-517112,
7 Andhra Pradesh, India

8 2. Dept. of Physics, University of Kashmir, Srinagar 190006, Jammu and Kashmir, India

9
10 *Corresponding author; Email: tkram@narl.gov.in

11
12 **Abstract**

13 As a joint research collaboration between the National Atmospheric Research
14 Laboratory (NARL), and the University of Kashmir (KU), NARL installed an all-sky airglow
15 CCD imager (with centre wavelengths of 630nm, 557.7nm [2nm band widths] and 840nm [150
16 nm wide band with blocking notch at 866 nm to avoid the contamination of molecular oxygen
17 emissions]) in the University campus in Srinagar (75E, 34N, geographic) Jammu and Kashmir,
18 India (western Himalayan region). To understand the upper atmospheric dynamics and
19 ionospheric electrodynamics and their associated physical coupling mechanisms, the imager
20 observes airglow emissions of OH molecules and atomic and molecular oxygen occurring at
21 the heights of ~80-300 km. First-time airglow observations in Kashmir commenced in the night
22 of August 11, 2017 and the present work reports on the characteristics of first-time observation
23 of Medium Scale Travelling Ionospheric Disturbances (MSTIDs with horizontal wavelengths
24 of ~100-300 km) which occurred during 20:30 - 22:30 hr. IST (Indian standard time) on August
25 15, 2017 (India independence day). Initially, the phase front of MSTIDs was aligned along the
26 north-west and south-east direction and moved at ~57 m/s towards the south-west direction and
27 finally the westward direction by aligning along the meridian before they disappeared. Along
28 with SAMI-3 ionospheric model simulations, simultaneous multiwavelength airglow
29 observations indicate that secondary gravity waves generated due to dissipation of upward
30 propagating mesospheric gravity waves in the heights of ~85-95 km would have contributed to
31 the generation of MSTIDs in the F region ionospheric plasma through electrodynamic
32 coupling between the E and F region (Perkins instability) ionosphere.

33 1. Introduction

34

35 Medium Scale Travelling Ionospheric Disturbances (MSTIDs) can be induced by
36 atmospheric gravity waves generated by wind flow over mountains, wind shears and jet
37 streams, auroral Joule heating effects and many other sources [Schunk and Nagy, 2000;
38 Jacobson and Erickson, 1992a, 1992b; Jacobson et al., 1995; Afraimovich et al., 2003; Kotake
39 et al., 2007; Tsugawa et al., 2007]. MSTIDs can be identified as mesoscale wave-like
40 perturbation of the ionospheric plasma with horizontal wavelengths of several hundred
41 kilometers, period of 15–60 min, and horizontal velocity of 100–250 m/s often observed in the
42 mid latitude F-region ionosphere [Francis, 1974; Hunsucker, 1982]. Using the data of 350 GPS
43 receivers of ionospheric total electron content obtained over Southern California, Kotate et al.
44 [2007]] studied in detail the statistical characteristics of MSTIDs. They categorized MSTIDs
45 into (1) daytime MSTIDs which can be generated due to atmospheric gravity waves in the
46 thermosphere mainly in winter and equinoxes and propagate mostly south eastward, (2) night
47 time MSTIDs occurring frequently in summer and propagating south westward, which is
48 consistent with the idea of polarization electric fields playing an important role in generating
49 night time MSTIDs, (3) dusk time MSTIDs occurring frequently in summer and propagating
50 north westward. Dusk time MSTIDs are thought to be caused by atmospheric gravity waves
51 originating from the sunset terminator as the wave fronts are almost parallel to the sunset
52 terminator. Airglow images obtained using high sensitive CCD cameras have revealed that
53 night time MSTIDs normally propagate southward (e.g., Mendillo et al., 1997; Kubota et al.,
54 2000; Garcia et al., 2000; Shiokawa et al., 2003a), which cannot be explained by the classical
55 theory of gravity waves (Miller et al., 1997; Kelley and Miller, 1997). Normally, day time/night
56 time MSTIDs occur frequently in winter/June solstice in the Japanese and Australian
57 longitudinal sector and near December solstice in the European longitudinal sector [Shiokawa
58 et al., 2003a; Herná'ndez-Pajares et al., 2006; Kotake et al., 2006, 2007]. Earlier studies over
59 Japan report that there is a good match between horizontal two-dimensional maps of total
60 electron content perturbations (TECp) as determined by Global Positioning System (GPS)
61 receivers and F region ionospheric 630 nm emissions [Saito et al., 2001; Ogawa et al., 2002].
62 Similar observations of both day and night time MSTIDs are also reported for the North
63 American region [Kotake et al., 2007; Tsugawa et al., 2007]. In addition, night time F region
64 field-aligned irregularities (FAIs) as observed by the MU radar in Japan also show high
65 correlation with MSTIDs activity, both propagated south-westward with same velocities [Saito

66 et al., 2001]. Night time MSTIDs occur mainly in the bottom side of the F region where the
67 peak emission rate of 630-nm airglow occurs at 250–260 km [Kubota et al., 2000; Ogawa et
68 al. 2002].

69
70 Some travelling ionospheric disturbances (TIDs) are identified as Travelling Wave
71 Packet TIDs (TWPTID) which is associated with atmospheric acoustic-gravity waves. GPS
72 based study of TWPTIDs indicates that they appear as quasi periodic wave packets with
73 Gaussian envelopes of width ~ 1 h modulated with periods of few tens of minutes [Afraimovich
74 et al., 2003]. Based on space based (COSMIC also known as FORMOSAT-3) observation of
75 ultra violet emissions from the ionosphere in conjunction with the Very Large Array (VLA)
76 radio telescope, located near Socorro, NM, Dymond et al. [2011] reported the observation of
77 MSTIDs. They observed the MSTIDs as waves with 23.8, 11.9, and 10.6 min periods having
78 speeds >200 ms^{-1} and traveling faster than typical night time MSTIDs speeds of ~ 100 – 150
79 m/s which are slower than the speed of sound in the thermosphere (~ 400 – 800 m s^{-1}) and are
80 within the speed range associated with MSTIDs [Hocke and Schlegel, 1996]. Further, their
81 VLA observations indicate the presence of MSTIDs with amplitudes of 0.14, 0.05, and 0.07
82 TECU (total electron content unit = 10^{16} electrons/ m^2) and with the corresponding horizontal
83 wavelengths of 239, 188, and 162 km. Using ground-based GPS receivers in the low latitude
84 region of Taiwan, earlier Lee et al. (2008) detected night time MSTIDs, with wave fronts
85 aligned along the northwest-southeast direction and with wavelength of ~ 500 km, moving
86 south westward to latitude of 20.5°N at the horizontal velocities between 100 and 160 m/s .
87 Further, their observations indicated that MSTIDs play important role in the generation of low-
88 latitude F-region ionospheric plasma irregularities.

89
90 Strong polarization electric fields found inside the structure of night time MSTIDs
91 indicate that Perkins instability could play a major role in the generation of night time MSTIDs
92 [Perkins, 1973; Garcia et al., 2000; Saito et al., 2002; Shiokawa et al., 2003b]. The Arecibo
93 incoherent scatter radar also detected intense polarization electric field associated with night-
94 time mid-latitude F-region ionospheric MSTIDs [Miller et al., 1997]. The earlier classical
95 theory of influences of atmospheric gravity waves on the generation of TIDs did not
96 incorporate the effect of disturbed polarization electric field generated in the F region
97 ionosphere (Hines, 1974). Perkins instability could successfully explain the normal observation
98 of northwest–southeast alignment of density perturbations associated with night time MSTIDs

99 [Yokoyama, et al., 2008]. However, it predicts the propagation direction of MSTIDs in the
100 north-eastward rather than the south-westward direction and the generated perturbation electric
101 fields aligned along the MSTID wave fronts could cause them to move south westward [Kotake
102 et al., 2007]. Various atmospheric and ionospheric phenomena like atmospheric gravity waves
103 [e.g., Hunsucker, 1982], electrodynamic coupling between F- and E regions [e.g., Otsuka et
104 al., 2007] and between two hemispheres [e.g., Otsuka et al., 2004; Shiokawa et al., 2005] is
105 considered as an important seeding mechanism of the Perkins instability. The restriction in the
106 southward propagation of MSTIDs beyond $\sim 20^\circ\text{N}$ is due to higher electron densities in the low
107 latitude regions as they can impede the southward advancement of atmospheric gravity waves
108 (seed of the wave-like structure of MSTIDs) through the ion-drag effect [Liu and Yeh, 1969;
109 Hines, 1972, Shiokawa et al., 2002, 2005]. The complex meso-scale structures of MSTIDs
110 indicate the existence of an unknown interaction between the neutral atmosphere and the
111 ionized plasma in the mid latitude ionosphere.

112

113 Given the complex scenario of MSTIDs, as a collaborative research effort between
114 NARL and the Dept. of Physics of University of Kashmir, Srinagar, Jammu and Kashmir,
115 India, NARL has installed one all-sky airglow imager in the University campus to study the
116 characteristics of mesospheric wave dynamics and the ionospheric electrodynamics in the
117 Indian subtropical region. Since the Kashmir region is located in the western Himalayan valley
118 region, it is expected that the atmospheric winds associated with subtropical jets can induce
119 different kinds of atmospheric gravity waves upon hitting the western Himalayan hills from
120 the west. The imager is operating at the centre wavelengths of (1) 630nm [atomic oxygen
121 emission with peak at $\sim 250\text{km}$], (2) 557.7nm [atomic oxygen emission with peak at $\sim 97\text{ km}$;
122 2nm band widths] and (3) 840 nm [OH emission (peak at $\sim 86\text{ km}$) with wide 200 nm band
123 width and notch filter at 868nm to get rid of contaminating molecular oxygen emissions from
124 the height of about 95 km). This paper delves on the linkage between the atmospheric gravity
125 waves observed at the height of $\sim 86\text{ km}$ and the travelling ionospheric disturbances namely
126 MSTIDs detected at the height of $\sim 250\text{km}$.

127

128 **2. Airglow CCD imager data processing and SAMI3 ionosphere model**

129

130 Using a circular medium format F/4 Mamiya fish-eye-lens (24 mm focal length), the
131 airglow CCD imager consists of a set of plano-convex lens in the front optics to make parallel

132 the rays of the collected light from space. These parallel rays are allowed to pass through
133 temperature controlled Fabry-Perot etalon (interference filters) which is normally maintained
134 at 25°C. Filters are located inside a filter wheel that can accommodate up to six 3-inch diameter
135 filters each with thickness of a quarter of an inch and they have 50-90 % transmission
136 coefficients. Filters corresponding to the centre wavelengths of 630nm (O¹D) and 557.7nm
137 (O¹S) have a narrow band width of about 2nm and the OH 840 nm filter is a 720-920 nm wide
138 band filter with blocking notch at ~868nm to get rid of the contaminating molecular oxygen
139 emissions. Separate narrow band filters with centre wavelengths of 866 and 868 nm are also
140 fitted in the filter wheel. At near infrared (NIR) wavelengths, etaloning effects in the CCD
141 camera are prominent and the data of which are not presented here as it requires further
142 treatment of received emission signals. The optical rays after passing through the filters are
143 allowed to pass through a relay optics system and finally they are collected on to a CCD camera
144 (PIXIS, Princeton Instruments) which contains a back illuminated e2vCCD47-10 chip
145 (ActonPixis1024B) with 1024×1024 square pixels each of which is having a size of 13.3
146 μm, 100% fill factor and 16-bit depth. The camera is cooled to -70°C to minimise dark noise.
147 In the present work, pixels are 2×2 bin averaged and hence finally the png format images
148 generated will have 512×512 array of 16-bit digitized data values. The experiments were
149 conducted by setting the scanning time of 100 seconds for the 630nm and 557.76nm filters and
150 10 seconds for the 840nm filter as it is a wide band filter through which more intense signals
151 of more wavelengths will propagate. The generated data images are then utilized for further
152 analyses and the results are presented. Further details of the instrument and data, methodology
153 of extraction of geographical coordinate information of various airglow emissions occurring at
154 different heights can be found in Garcia et al. [1997], Kubota et al. [2001], Alok et al. [2013].
155 The present work adopted the image processing algorithms as mentioned in Alok et al. [2013].

156

157 **Imager data processing:**

158

159 Using the relationship between the coordinates of the fish-eye-lens of the front optical
160 system of the imager (zenith angle θ and azimuthal angle ϕ) and the geography of the imager
161 site for a particular height in the atmosphere (horizontal distance r from the centre of the site
162 and the azimuthal angle), the obtained raw images are un-warped to determine the geographical
163 coordinates of particular interests of atmospheric and ionospheric information [Kubota et al.,
164 2001].

165 $r = R_E \times \alpha$

166 $\alpha = \theta - \sin^{-1}(R_E \times \sin\theta / (R_E + h_{ag}))$

167

168 where θ is the zenith angle, R_E is the radius of the Earth and h_{ag} is the altitude and r is the
 169 horizontal radial distance from the centre of the image (site location) to the point of interest
 170 corresponding to the zenith angle (geographical spatial information) of the airglow emission
 171 layer.

172

173 With this information of geographical coordinates of all the pixels of the observed
 174 image data and time sequenced images, the horizontal wavelength, period and phase speed and
 175 direction of moving phase fronts of atmospheric gravity waves or ionospheric plasma
 176 irregularity waves manifested in intensities of airglow emissions can be determined. Further,
 177 the phase speed of waves can be obtained from keograms by choosing a line along a particular
 178 phase front and calculating its slope from both the zonal and meridional keograms. This gives
 179 us the two components of phase velocities. e.g for a SW moving wave we get southward
 180 component from meridional keogram and westward component from the zonal keogram. Then
 181 the resultant phase velocity of the wave event is given by

182
$$v_p = \sqrt{v_m^2 + v_z^2},$$

183 where v_m = meridional phase velocity component and

184 v_z = zonal phase velocity component.

185

186 By knowing the time period from time series of images, we can easily determine the
 187 horizontal wavelength from the knowledge of horizontal phase velocity.

188

189 Since the optical system can introduce nonuniformities in the distribution of recorded
 190 airglow emission intensity across all the pixels, firstly it needs to be corrected (flat field
 191 correction) before proceeding for further analyses. Using imager calibration data for each of
 192 the wavelengths of optical filters supplied by Keo-Scientific (manufacturer of the imager),
 193 enough care has been taken to remove the non-uniformities in the present work. As a result,
 194 the intensity values are given in SI units as $\text{Watt sr}^{-1} \text{m}^{-2}$ which can be converted in to rayleigh
 195 units through the equation [Baker and Romick, 1976].

196

197 For example,

198 Wavelength, $\lambda = 630\text{nm} = 0.63 \mu\text{m}$

199 $1 \text{ rayleigh} = 10^{-9}/2\pi\lambda \text{ W sr}^{-1} \text{ m}^{-2} = 10^{-3}/2\pi 0.63 \text{ W sr}^{-1} \text{ m}^{-2} = 0.25 \times 10^{-3} \text{ W sr}^{-1} \text{ m}^{-2}$

200 Radiance, $L = 0.01 \text{ W sr}^{-1} \text{ m}^{-2}$ (typical from Fig. 2 of the present work)

201 $L = 0.01 \text{ W sr}^{-1} \text{ m}^{-2} = 10 \times 10^{-3} \text{ W sr}^{-1} \text{ m}^{-2} = 40 \text{ rayleigh}$

202

203 Apart from this non-uniformity, for a particular wavelength, airglow intensity
 204 decreases for the off-zenith rays approaching the front optics from the side of the lens compared
 205 to the zenith rays. However, at low elevation angles in the sides of fish eye lens, thicker airglow
 206 emission layer leads to increase in intensity (Van Rhijn effect) and thus partially compensates
 207 for the loss due to oblique incidence of the rays. If we remove (say few hours of observation
 208 on a particular day) all pixels-averaged signal from the original raw signal of each and every
 209 pixel in a particular frame, the remaining other nonuniformities also will be significantly
 210 removed. Similar methodology is adopted in the present work and nonuniformities are largely
 211 removed except for strong signals associated with stars and galaxies, which can be easily
 212 distinguished from the atmospheric features.

213

214 Atmospheric wave motions and their essential wave parameters like horizontal
 215 wavelength, phase speed and direction are determined by identifying their bright bands (intense
 216 airglow emissions associated with crest of wave motions) and their spatial separations as well
 217 as their time evolutions in time series of images. Wave front moving direction can easily be
 218 identified in the un-warped images which contain geographical coordinate information at a
 219 particular height corresponding to particular wavelength of airglow emission associated with
 220 that height region. Since the gravity wave phase speed is determined by noticing the time
 221 movement of high intense bands associated with crest of gravity waves in space (geographical
 222 coordinate mapping in images), errors in the calculation of wave speed arises due to the time
 223 evolving diffusion of these intense bands that have sizeable widths in space. Taking this into
 224 account the roughly estimated errors in wave speed and wavelength are provided in closed
 225 brackets along with actual speed values wherever mentioned in the remaining text.

226

227 **SAMI3 ionosphere model description:**

228 In a unique, non-uniform, non-orthogonal and fixed grid, the Naval Research
 229 Laboratory (NRL) ionospheric plasma model SAMI3 [Huba and Krall, 2013] is a three-

230 dimensional global model based on its earlier two-dimensional model SAMI2 [Huba *et al.*,
231 2000, 2008]. The SAMI3 calculates these ions densities: H^+ , He^+ , N^+ , O^+ , NO^+ , N_2^+ and O_2^+
232 ions in the heights of 85 km to 20,000 km and it is well suited for the studies of MSTIDs also
233 as its updated version includes the information of mesospheric gravity waves that lead to the
234 generation of MSTIDs (Huba and Krall, 2013). Further SAMI3 solves electron and ion
235 temperature equations for H^+ , He^+ , and O^+ ions by including ion inertia in the ion momentum
236 equation along the geomagnetic (offset and tilted dipole) field lines. It offers modelling of the
237 ionospheric plasma from hemisphere to hemisphere by employing ionospheric flux tube model.
238 The information of vertical and zonal drifts of the ionospheric plasma due to $\mathbf{E} \times \mathbf{B}$ drifts
239 associated with zonal (vertical drifts) and meridional (zonal drifts) electric fields is also
240 included. While NRLMSISE00 model provides information of neutral composition and
241 temperature, HWM model provides the neutral wind information as background input neutral
242 atmospheric parameters for running the SAMI3 full physics model. More detailed information
243 of the SAMI3 model data can be obtained from the website
244 <https://ccmc.gsfc.nasa.gov/models/modelinfo.php?model=SAMI3>.

245

246 3. Observations and results

247

248 Figure 1 shows the NARL all-sky airglow imager observations of 630 nm emission, by
249 atomic oxygen at the height of about 250 km in the F region ionosphere over the Indian
250 subtropical station of University of Kashmir (75E, 34N, geographic; magnetic latitude ~ 26 N;
251 ~ 4000 m above mean sea level), Srinagar, Jammu and Kashmir, on 15 August 2017. In total,
252 there are 28 panels of figures, each of which is obtained for an individual scan period of 100
253 seconds starting from 20:33 hr. IST (Indian Standard Time = UT+5:30hr) onwards and the time
254 interval between two panel is about 4 minutes. It can be noticed that the top and left most panel
255 (20:33 hr. IST) shows diffused dark bands and in the subsequent panels the bands appear
256 moving towards the south-west direction. The bands (phase fronts) are aligned along the north-
257 west and south-east directions and the normal to these bands move towards the south-west
258 direction. With time, multiple bands arrive in the field of view of the imager and move towards
259 the south-west direction. There are three dark bands easily visible until 21:27 hr. IST and
260 afterwards only two bands are visible with the last band appearing at further distance from its
261 nearby band compared to other inter-band distances. It can also be noted that the bands start to
262 align along the north-south direction (meridian) as time progresses. At 22:27 hr. IST, the bands

263 are aligned almost parallel to the North-South direction. The last wider dark band, aligned
264 along the meridian, continues to move towards the west at 22:27 hr. IST. After reaching the
265 centre of the image (over head of Srinagar), the dark band widens with time and at 22:59 hr.
266 IST, the dark band expanded in such a way that the whole image appears dark with no
267 signatures of movement.

268

269 Figure 2 shows unwarped images of four panels of Fig. 1 in geographical coordinates
270 (covering the pixel number ranges of 101:400 and 101:400 in the east-west and north-south
271 directions respectively). They cover the horizontal space of $\pm \sim 700$ km in the north-south
272 direction (y-axis) and in the east-west direction (x-axis) at the height of ~ 250 km over KU,
273 Srinagar. This is in contrast to that of Figure 1 which is in pixel coordinate (512 by 512). The
274 image size is truncated to the pixels range 101-400 (instead of 1-512) which corresponds to
275 maximum zenith angle (field of view) of $\sim 57^\circ$ for all the three filters to avoid unnecessary
276 interfering signals (say surrounding street lights, buildings, trees) coming from nearby ground
277 locations surrounding the imager site. Important quantitative information like (1) inter-band
278 separation distance or horizontal wavelength, (2) band moving speed and direction and their
279 time evolution is extracted from these images. It is also illustrated in Fig. 2 as to how the
280 horizontal wavelength, speed and direction are estimated. It is observed that initially the
281 horizontal wavelength (spatial separation between two white or dark bands) observed is about
282 200 km ($\sim \pm 15$ km, Fig. 2a) and within half an hour it became about 180 km ($\sim \pm 10$ km, Fig. 2b)
283 and in the next half an hour it became about 60 km (± 8 km, Fig. 2c). In the next half an hour,
284 the waves begin to disappear. As the bands cover the whole image, it is estimated that the total
285 length of each of the bands is of the order of 900 km. Since the horizontal wavelength is
286 significantly varying with time, it is difficult to find the exact speed of the moving phase front
287 of these MSTIDs. The calculated speed of the phase front turns out to be around 57 m/s ($\sim \pm 5$
288 m/s). The four panels in this figure (Fig. 2) are separated in time by about half an hour
289 beginning at 20:33 hr. IST. The intensity values are obtained by taking in to account of the
290 calibration of the imager at 630 nm but with band width of about 2nm. The Van Rhijn and
291 atmospheric extinction effects in the images are partially corrected by removing averaged
292 signal strength from each of the pixels as these effects do not influence the interpretation of the
293 physical structure of the observed MSTIDs in any significant way. Removing them is,
294 therefore, inconsequential.

295

296 Figure 3 illustrates the keogram images of 630 nm emissions at ~250 km height that
 297 occurred on the night of 15 August 2017. While the x axes show the time period of observation,
 298 the y axes show the west-east evolution of north-south averaged 50 pixels. The horizontal
 299 north-south space covering 50 pixels is indicated on the top of the corresponding panels in
 300 which negative values denote the southern side of the imager location. The top and left most
 301 panel shows the southern side averaged (179-326 km in the south side of the imager at 250 km
 302 height) intensity of the 630 nm emission and its time as well as east-west spatial evolution. It
 303 can be easily identified that in the first one hour (20:30-21:30 hr IST as observed in the Figure
 304 1), there is well-defined bright patterns of intensity moving towards the west. In the next right-
 305 side panel, covering the 84-179 km region in the South, it seems that there is an increase in the
 306 number of patterns in the east-west direction. The interesting thing to be observed here is that
 307 the intensity of these patterns gradually reduces in the northern side of the imager as noted in
 308 the bottom panels (Figure 3). Also, it can be noted that the well-defined patterns of four bands
 309 in the southern (top panel) side averaged intensity got diffused in the northern side (bottom
 310 panel). The estimated zonal wavelength is ~225 km (± 15 km) and the phase front observed
 311 westward speed is about 50 m/s ($\sim \pm 5$ m/s). Actually, different bands show variable zonal phase
 312 speeds. Bands located in the far western side of the imager site shows westward phase speed
 313 of about 20 m/s ($\sim \pm 4$ m/s) but those located near the zenith of the site shows large phase speed
 314 of about 50 m/s ($\sim \pm 5$ m/s). Bands located in the far eastern side of the imager shows about 25
 315 m/s ($\sim \pm 6$ m/s). Wave activities are seen until about 22 hr. IST. Again, here, it can be noticed
 316 that the phase speed becomes slower with time and finally they moved mostly in the west
 317 direction with minimum speed. One more thing to be noticed here is that there are four bands
 318 visible in the first hour of observation (top middle panel in Fig. 3). The bottom most band,
 319 located and aligned along the west side of the imager, remained almost stationary and all other
 320 bands move westward with increasing speed in the eastward direction (bright band). The band
 321 structures appear to move mostly westward and the band patterns are similar in the northern
 322 and southern most averaged plots. Further, after 21:10 hr IST, the bands intensities reduced
 323 with time and finally around 22:40 all bands disappeared.

324
 325 Figure 4 illustrates the same as Figure 3 except that here north-south and east-west
 326 directions are interchanged. In the southern side of the imager (-ve y axis), the well-defined
 327 strong intensity bands move towards the south in the first one hour with southward phase speed
 328 of about 110 m/s ($\sim \pm 10$ m/s), meridional wavelength of ~200 km zonal wavelength of ~200
 329 km and horizontal wavelength of about 142 km ($\sim \pm 10$ km). In addition to this, in the first hour,

330 there are small scale bands which move towards the north in the northern side (+ve y axes) of
331 the imager. These features though weak extend for another one hour. The source mechanism
332 of this northward moving small-scale bands might be due to the unstable ionospheric plasma
333 conditions developed in the large-scale MSTIDS moving in the south-westward direction.
334 Because the perturbed electric fields associated with MSTIDs and the earth's magnetic field
335 together can generate $E \times B$ drift of the plasma that flows orthogonal to the primary electric field
336 of MSTIDs. In addition, there are beaded string (21:48-22:24 IST) types of intensities with
337 signatures of movement in time from $\sim 21:40$ hr IST onwards, which are nothing but signals
338 associated either with stars or cloud motions occurring in the lower atmosphere. In order to
339 find whether the movement of observed band patterns towards the west or south is a regular
340 phenomenon, the same analysis was carried out for the next day also i.e. August 16, 2017. No
341 such wave pattern was observed on the August 16 night.

342

343

344 **4. Discussion and conclusions**

345

346 From Figure 1, one important observation is that after the dark and bright bands of 630nm
347 emission are aligned along the N-S direction, the bands lose their distinct shape and expand in
348 the east-west direction and finally all the bands either disappear or merge into a single one
349 marking the end of the life of TIDs or specifically MSTIDS as in the present case. It is to be
350 recalled that while the Perkins instability makes the bands to align along the north-west and
351 south-east directions, it is either the southward moving winds or winds associated with
352 southward propagating atmospheric gravity waves that make these bands to move in the south-
353 west ward direction in night times. While moving so, the earth's magnetic field slowly tries to
354 control the time evolving plasma bands through time evolving perturbation electric field as its
355 strength and hence the strength of $E \times B$ drift speed increases with time. This would make both
356 the inter band spacing and the band width, particularly the dark bands, to increase. Once these
357 bands get aligned along the N-S direction, they come under the full control of the earth's
358 magnetic field. This may be one of the major reasons that the initial south-westward motion of
359 MSTIDs finally becomes westward motion and then they dissipate. These mechanisms are well
360 illustrated in all the panels of Figure 1.

361

362 Now the source of the atmospheric gravity waves needs to be taken in to account. Figure 5
363 is identical to Figure 3 except that it is now the airglow emissions at the centre wavelength of
364 840 nm associated with OH molecular emissions occurring at the height of about 86 km. It is
365 interesting to note here that similar to Figure 3 for atomic oxygen emissions at ~250 km height,
366 OH emissions at 86 km (top and left most panel in Fig. 5) also show similar and distinct band
367 patterns of bright emissions moving westward (~5 m/s) in the first one hour of observations.
368 Fig.6 shows the same as in Fig. 5 except that it is now 50 bins averaged in the east-west
369 direction and the features moving (~2.5m/s) southward. The southward motion of bright
370 patches of 840 nm emission intensity clearly indicates that the mesospheric gravity waves
371 observed in the present work at the height of ~86 km propagated in the south-westward
372 direction with moving speed of ~5.6 m/s. Figure 7 shows the same as Figure 5 but for the
373 557.7nm emission by atomic oxygen at the height of about 97 km. Similar to the Figures 3 and
374 5, Figure 7 (557 nm emissions in the height of ~97 km) also shows that there is a kind of band
375 pattern moving westward in the first two hours in the southern side averaged (top panel)
376 intensities. The north ward moving band patterns visible in Figure 8, which is for the 557.7nm
377 emission and is same as Figure 6 except for the 840 nm emission, are thought to be due to in-
378 situ generated gravity waves.

379

380 The simultaneous occurrence of bright and dark bands in all the three wavelengths (at the
381 heights of ~86km, ~97km and ~250 km) in the first one hour of the present observation period
382 would indicate that mesospheric gravity waves would have contributed to the appearance of
383 MSTIDs in the F region ionospheric plasma. To our knowledge, this result is first of its kind
384 showing simultaneous occurrence of west ward moving airglow band at the heights ranging
385 from 85 km to about 250 km. The present observation of northward (Figure 8) moving patterns
386 of 557.7 nm emission at ~97 km, southward (Figure 6) moving patterns (many bands) of 840
387 nm emission at ~85 km and the south ward (Figure 3) moving ionospheric plasma at ~250 km
388 (only a few bands associated with MSTIDs) raises an important question that how the MLT
389 region (mesosphere and lower thermosphere) small horizontal wavelength atmospheric gravity
390 waves would have led to generation of large horizontal wavelength MSTIDs in the F-region
391 ionosphere. Further, Perkins instability mechanism demands southward moving winds to
392 generate the south-westward propagating MSTIDs (Jonah et al. 2016). The southward moving
393 atmospheric gravity waves in the mesosphere can lead to the generation of MSTIDs. To explain

394 this, we calculated the vertical wavelength of the gravity waves observed in the 840 nm
395 emission (~85 km height) by using the gravity wave dispersion relation (Hines, 1960)

$$396 \quad m^2 = N^2/(U-c)^2 - k^2 - 1/4H^2 \quad \text{----- (1)}$$

397 where $m = 2\pi/\lambda_z$ is the vertical wave number of gravity waves

398 $N = 2\pi/T$ is the Brunt-Vaisala (BV) frequency and T is the BV period ~ 6 minutes in the
399 mesosphere region near 85 km

400 k = horizontal wavelength; H is the atmospheric temperature scale height ~ 8 km in the
401 mesosphere.

402 In the present work it is obtained ~25 km and ~15 km as zonal wavelength (0.04 per km
403 wavenumber) and meridional wavelength (0.06 per km wavenumber) respectively. The
404 horizontal wavenumber is $= \sqrt{(0.04*0.04)+(0.06*0.06)} = \sqrt{0.0016+0.0036}$
405 $=\sqrt{0.0052} = 0.07$; horizontal wavelength = $1/0.07 = 14.2$ km

406 Here c , phase speed of the gravity waves and k can be obtained from the imager data of OH
407 emissions in the height of ~85 km.

408 The values obtained from the analyses of the images of the present work are:

$$409 \quad c = -5 \text{ m/s (present OH image data)}$$

$$410 \quad k = 2\pi/14.2 \text{ km (present OH image data)}$$

$$411 \quad U = -90 \text{ m/s (TIDI (TIMED satellite data for the height of ~85 km))}$$

412 Please see the height range of 82-90 km in Fig. 9 in which except for one profile (76E,
413 39N) all the other four profiles show values (negative) more than 90 m/s and within up to about
414 175 m/s.

415 With these values inserted in equation 1, the value of the square of the vertical wavenumber
416 becomes negative and hence these waves can be classified as external or transient gravity
417 waves that cannot propagate above this height of ~ 85 km. It is interesting to note here that at
418 the height of ~97 km (Figs. 7 & 8, atomic oxygen emission, 557.7nm), the southward
419 propagating gravity waves observed in the heights of ~85 km (OH emission; 840 nm) is
420 disappeared but there is a presence of northward propagating waves. It is interesting to
421 understand what would have happened to the mesospheric (~85 km) gravity waves in the lower

422 thermosphere (~97 km) and how other new gravity waves generated there at ~97 km height.?
423 Fig. 9 indicates that the strong negative wind speed (south-west ward) changes its direction
424 around ~90 km height and becomes positive (north-east ward) above about 97 km height. It is
425 speculated here that this strong wind shear in the heights of 90-97 km would have led to the
426 dissipation of the gravity waves observed in the mesospheric heights of ~85 km. The observed
427 northward moving gravity waves at ~97 km height is possibly due to in-situ generated
428 secondary gravity waves that arose due to either dissipation of the upward propagating
429 mesospheric gravity waves or any other tides or planetary waves or a mixed of all these waves.
430 It is taken as a future exercise to determine the exact source mechanism of the northward
431 propagating gravity waves in the height of ~97 km during the first few hours of observation on
432 15 August 2017. It seems that the secondary gravity waves observed in the height of ~97 km
433 would have been dissipated in the higher heights of about 105 km (Fig. 9) as there is another
434 strong vertical shear of horizontal wind near this height (reversal of wind near 105 km in Fig.
435 9).

436

437 Given this scenario of observation of gravity waves near the height of ~85 km (OH
438 emission, 840 nm, Figs. 5 & 6) and their dissipation in the higher heights of about 97 km and
439 the generation of secondary gravity waves at this height along with their possible dissipation
440 around 105 km, how could atmospheric gravity waves would have contributed to the generation
441 of MSTIDS in the present study. This is an intriguing question that demands convincing
442 answers to explain the exact generation mechanisms of MSTIDS. Here it is needed the
443 knowledge of basic physical principles of generation of both the MSTIDs and the contribution
444 of atmospheric gravity waves to them for their growth in the F region ionosphere. Full physics-
445 based model simulations of generation and dissipation of atmospheric gravity waves and their
446 coupling with ionospheric plasma physics can shed light on this issue. Fig. 12a shows the
447 SAMI3 ionosphere model results of height profiles (85-150 km) of electron density and their
448 time evolution (13:30 – 24:00 UT; 19:00 – 05:30 IST on 15 August 2017) over the CCD imager
449 site of Srinagar. It can be observed that above the height of 85 km and up to the height of about
450 110 km, the electron density varies at high frequencies (time) comparing to those at heights
451 higher than 110 km. This would indicate that direct influences of mesospheric and lower
452 thermospheric gravity waves on the ionospheric plasma would have been limited to heights
453 below 110 km. Above this height, secondary gravity waves generated through dissipation of
454 upward propagating lower atmospheric gravity waves could be one of important source

455 mechanisms of periodic motions in ionospheric plasma irregularities. The influences of these
456 secondary waves on ionospheric plasma can be seen even up to above the peak (electron
457 density) of the F region ionosphere. Fig. 12b illustrates this phenomenon clearly; here one can
458 see the influence up to the height of ~ 500 km. Fig. 13 illustrates the time evolution of horizontal
459 map of (60E-90E; 20N-50N; geographic) SAMI3 model electron density at the height of 125
460 km where the signature of MSTIDs started to be visible from below. As the centre of this figure
461 approximately matches the location of the CCD imager site, Srinagar (75E, 34N; geographic),
462 it can be seen clearly how the periodic variation of electron density portrayed. At 13:30 UT
463 (19:00 IST, Fig. 13a), there is no clear periodic variation of electron density noticed except for
464 its gradual decrease with longitude which is normal and expected as our earth rotates and hence
465 decreasing ionizing radiation from sun for the E region ionosphere. Oscillating patterns started
466 to be visible at 14:30 UT (Fig. 13c) and at 15:00 UT (Fig. 13d) it is clearly seen the oscillations
467 in electron density in the latitude region of ~ 37 -45 N. The oscillating patterns, drifting mostly
468 westward with time, is disappeared at 16:30 UT (22:00 IST, Fig. 13g) in regions beyond 67E.
469 The present imager data also showed similar time variations of MSTID (Fig. 1). This shows
470 that the SAMI3 model finely reproduced the MSTID structures as observed by the CCD imager
471 over Srinagar.

472

473 **Secondary gravity waves leading to generation of MSTIDs**

474

475 As the mesospheric and lower thermospheric gravity waves seen in the heights of ~ 85
476 km and ~ 97 km would have possibly dissipated below ~ 105 km because of the strong wind
477 shears at the heights of ~ 90 km and ~ 105 km, it is imperative to find a logic reason to link these
478 observed waves with simultaneous appearance of MSTIDs over the CCD imager site of
479 Srinagar. As an interesting work supporting the present observations, Vadas and Liu (2009)
480 reported the generation of fast- and large-scale secondary gravity waves in the lower
481 thermosphere from the dissipation of upward propagating lower atmospheric convectively-
482 generated slow-moving small and medium scale gravity waves. Using the high-resolution
483 NCAR Thermosphere-Ionosphere-Mesosphere-Electrodynamics General Circulation Model
484 (TIME-GCM) they studied the response of the thermosphere and ionosphere to the dissipation
485 of the gravity waves generated from a single deep convection in the lower atmosphere. They
486 successfully simulated the generation of large scale travelling ionospheric disturbances

487 (LSTIDs) due to the propagation of the excited, large-scale, secondary GWs with horizontal
488 wavelengths of the order of more than 2000 km in the heights of 120-250 km. The convectively
489 generated gravity waves had horizontal wavelength of ~40–150 km, vertical wavelength of 50–
490 65 km, and period of 10–20 min and their dissipation in the lower thermosphere led to the
491 generation of secondary gravity waves with horizontal wavelength of the order of 2000 km,
492 period of 80 min and horizontal speed of 480-510 m/s. Similar further studies by Vadas and
493 Liu (2013), Vadas and Crowley (2010), Vadas (2013) also reported excitation of secondary
494 gravity waves with horizontal wavelengths of ~100-4000 km and phase speeds of ~100-500
495 m/s in the heights of 120-250 km due to dissipation of upward propagating gravity waves. It is
496 also claimed that these secondary large- scale gravity waves can propagate globally and
497 vertically beyond above 400 km and induce moving ionospheric plasma disturbances like
498 MSTIDs or LSTIDs [Vadas and Liu, 2013; Liu and Vadas, 2013].

499

500 For the present report, it can be argued that the simultaneous occurrence of MSTIDs in the
501 ionosphere and the gravity waves in the mesosphere (OH, 85 km) and lower thermosphere (O,
502 97 km) can be completely independent of each other. To strengthen the point of view that they
503 are strongly linked to each other, one can compare the time period and evolution of the
504 mesospheric gravity waves (Fig. 5) and MSTIDs (Fig.3). It is outstandingly matching and both
505 the signals lose their significance after 22 hrs IST. Then the next question to be addressed here
506 is that when gravity waves take hours to reach the ionosphere from the mesosphere, how can
507 they simultaneously be present. It is to be noted here is that the south-west ward propagating
508 gravity waves detected at ~85 km are evanescent ones (m^2 is negative at ~85 km height where
509 the waves were detected in the imager as mentioned above) and the strong wind shear in the
510 heights of 85-95 km (Fig. 9) would have dissipated them there. The turbulence generated thus
511 would have generated secondary gravity waves above about 100 km and these secondary
512 gravity waves would have influenced the E region electric field leading to the appearance of
513 MSTIDs in the SAMI 3 model (Figs. 11 and 12). At around 22:30 IST, the simultaneous
514 disappearance of MSTIDs in the 630nm emission (Fig. 3) and in the SAMI3 electron density
515 (Fig. 13g) and gravity waves in the mesosphere (Fig.5) over the Srinagar site (75E) clearly
516 illustrates that they strongly related to each other. Furthermore, if the observed MSTIDs were
517 generated somewhere in the mid latitudes and they just travelled over Srinagar, then they
518 should be still travelling and visible in the SAMI 3 model (Fig. 13g). But they disappeared in
519 all the observations simultaneously.

520 Another interesting feature is the observation of a secondary generation of ionospheric
521 plasma motions that move in the northward direction (Figure 4) in contrast to the MSTID
522 motion which is in the southward direction. The more interesting characteristic of the
523 secondary plasma motion is that it is restricted to be only generated in the northern side of the
524 imager site. A further detailed analysis of this observation will surely lead to more
525 understanding of the characteristics of locally generated MSTIDs, which is also taken as the
526 future scope of the present study.

527

528 **Western Himalayan topography link with mesospheric gravity waves**

529

530 Since the filter with 840nm as central frequency is actually a wide band (~720-920 nm with
531 blocking notch at ~866 nm) filter in the near infra-red (NIR) region, its scan time is only ten
532 seconds otherwise the receiver CCD camera would be saturated. As the lower atmospheric
533 cloud patches can emit strong NIR signals, it is possible to determine their horizontal velocities
534 by assuming that they are located at around 5 km height. Exact height determination of cloud
535 patch heights is possible by triangulation method but it needs a minimum of three imagers
536 separated in location by tens of kilometres distance. With single imager there may be error in
537 the assumption of 5 km height of the clouds but the determination of speed of clouds will not
538 change drastically as the clouds are normally spread within few kilometres of height. So, it is
539 reasonable to assume that the cloud patches observed in the 840 nm filter are at 5 km height.
540 As a result, the signals obtained using this filter will contain both the OH emission from the
541 height of ~86 km as well as the emissions from cloud patches in the lower atmosphere. In
542 Figure 6, for the keogram of time evolution of north-south spread of emissions of 840 nm
543 averaged in the east-west direction, it can be easily identified that there are many series of small
544 blobs of high intensities moving towards the north direction with more intensity in the eastern
545 side (top panel of Figure 6) of the imager. By assuming that the cloud patches are located at
546 the height of about 5 km, the northward speed of the clouds is estimated to be about 12 m/s
547 ($\sim\pm 2$ m/s), which is obtained from the rough measurement of time taken by a single cloud patch
548 (thick blob of high intensity) to move from the south to north end as in the top middle panel of
549 the Figure 6. This is in excellent agreement with ERA-5 reanalyses meridional wind velocity
550 at 5 km (Fig. 10d) over the Kashmir region. Fig. 11 shows the topography of the Kashmir
551 region corresponding to Figure 10. It seems that northward moving winds (Figure 10d) in the

552 lower atmosphere would have generated the lower atmospheric gravity waves by hitting over
553 the Himalayan mountain range from the south. Wind disturbances created in the upwind
554 streamside because of the wind flow from the south to the north would have converted into
555 southward propagating gravity waves in the higher heights and propagated vertically up into
556 the mesosphere and lower thermosphere region over Srinagar (upwind streamside valley
557 region). This may be one of the reasons that MSTIDs are more intense (top panel in Fig. 3) in
558 the southern side of the imager rather than in the northern side in the present work. This would
559 lead to the speculation that the MSTIDs reported in the present work were not generated in the
560 mid latitude region but they occurred as a result of lower atmospheric gravity waves generated
561 due to the effect of wind-flows over topography of mountains of the western Himalayas in the
562 Kashmir region. The observed gravity wave patterns in the mesospheric heights (840nm, Fig.
563 5) of about 86 km further supports our inference that it is the locally generated atmospheric
564 gravity waves that led to the generation of MSTIDs over the Kashmir region.

565 Normally, it is believed that topography generated gravity waves will have zero phase
566 speeds but the present observed mesospheric gravity waves possess phase speeds of about -35
567 m/s (± 5 m/s). Then question arises as to how the high phase speed gravity waves observed in
568 the mesosphere can be associated with topography in the lower atmosphere. If wind flows over
569 mountains generate non-hydrostatic gravity waves then they will have phase speeds depending
570 on the wave generation mechanisms and the background atmospheric wind and temperature
571 conditions in which the waves are generated and propagated [Bacmeister and Schoeberl, 1989].
572 If hydrostatic gravity waves are generated then they will have stationary phase speeds. Here
573 we don't know what kind of gravity waves were generated because of wind flows over the
574 Himalayas in the lower troposphere. Determining the gravity waves characteristics generated
575 in the lower atmosphere needs lot of atmospheric wind and temperature information
576 surrounding the Himalayas as well as in the higher levels of the atmosphere where the waves
577 are propagating vertically upwards. As we don't have observational information regarding
578 these physical processes, it is speculated that the gravity waves generated there would have
579 non-hydrostatic character and acquired high speeds in the mesosphere. Model simulations can
580 help but that is beyond the scope of the present work and it is taken as future scope. However,
581 the basic question here is that whether this wind speed of about 12 m/s at about 5km height
582 near the CCD imager site of Srinagar is sufficient for the generation of atmospheric gravity
583 waves in the troposphere. Durran (1990) showed how this parameter, NH/U where N is the
584 Brunt-Vaisala frequency, H is the height of mountain and U is the background wind speed, can

585 shed light on whether gravity waves can be generated with the given wind velocity and
586 mountain height.

587 For a bell-shaped mountain (with height H km) in the troposphere,

$$588 \quad N = 1/B_T = 1/5 \times 60 = 1/300 = 0.0033 \text{ (typical in the troposphere)}$$

589 where B_T is the Brunt-Vaisala period.

$$590 \quad H = \sim 4 \text{ km} = 4000 \text{ m (Fig. 11)}$$

$$591 \quad U = \sim 12 \text{ m/s (Fig. 10)}$$

$$592 \quad NH/U = 0.0033 \times 4000/12 = 1.11$$

593 According to Durran (1990), this value of $NH/U = 1.11$ can lead easily to generate vertically
594 and horizontally propagating gravity waves and hence it can be said that the lower atmospheric
595 topography and wind conditions near the CCD imager site of Srinagar were well suited for the
596 generation of atmospheric gravity waves that can propagate vertically up into the mesosphere.

597

598

599 **Acknowledgements:**

600 This work is supported by the Dept. of Space, Govt. of India. The Ph. D. enrolled
601 student Mr. Aashiq Hussain Bhat (AHB) expresses his sincere thanks to the organisers of ISEA-
602 15 for providing him financial assistance to participate and present the paper in the ISEA-15
603 symposium held in Ahmedabad, India and to the Dept. of Science and Technology for awarding
604 him INSPIRE Ph. D. fellowship. The other Ph. D. enrolled student Mr. Bilal Ahmad Ganaie
605 (BAG) thanks the UGC-CSIR of India for awarding him Ph. D. fellowship. Special thanks are
606 due to Prof. A. Jayaraman, the then Director of NARL and Prof. Khurshid Iqbal Andrabi, the
607 then Vice-Chancellor of the University of Kashmir for their keen interest and enormous support
608 that helped us to install the airglow imager and starting the airglow observations in Kashmir
609 for the studies of upper atmosphere and ionosphere. MAM, BAG and AHB are grateful to the
610 present Director, NARL, Dr. A. K. Patra for his support and permission granted to visit NARL.

611

612

613 **Data availability and accessibility**

614 While the ERA-5 data can be obtained from the website of
615 <https://cds.climate.copernicus.eu/cdsapp#!/dataset/reanalysis-era5-pressure-levels?tab=form>,
616 the ISRO-Bhuvan topographic data can be obtained from
617 https://bhuvan.nrsc.gov.in/bhuvan_links.php. The TIDI-TIMED satellite data can be accessed

618 from the website of <http://timed.hao.ucar.edu/tidi/data.html>. The airglow imager data are
 619 available in the institutional repository and they can be accessed via the institute (National
 620 Atmospheric Research Laboratory, NARL) website of <https://www.narl.gov.in>. The complete
 621 data archiving in this institute (NARL) website is underway and will be made available to the
 622 public in the near future. SAMI 3 model data are available at
 623 <https://ccmc.gsfc.nasa.gov/models/modelinfo.php?model=SAMI3> (last visited on 16 June
 624 2020)

625

626

627 **Figure legends**

628

629 **Figure 1** shows 36 panels (scans) of all-sky airglow images taken with NARL CCD imager at
 630 630 nm (2nm band width) for atomic oxygen emissions at ~250 km height in the campus of
 631 University of Kashmir (KU), Srinagar, Jammu and Kashmir, India on 15 August 2017. The
 632 scan time is 100 seconds and the time interval of the scans is about 4 minutes.

633

634 **Figure 2** illustrates the rectilinear-geographical spatial information of 630 nm emissions as
 635 shown in Fig. 1 (on 15 August 2017) for four scans separated by half an hour. While the y axes
 636 (zenith angle of $-57^\circ - 57^\circ$) run from South (bottom) to North (top), the x axes (zenith angle of
 637 $-57^\circ - 57^\circ$) run from West (left) to East (right) centred over KU, Srinagar. The colour bar
 638 values (emission intensity) are given in $\text{W sr}^{-1} \text{m}^{-2}$ which can be converted into Rayleigh unit
 639 as $1 \text{ Rayleigh} = 10^{-9}/2\pi\lambda \text{ W sr}^{-1} \text{m}^{-2} = 10^{-3}/2\pi \cdot 0.63 \text{ W sr}^{-1} \text{m}^{-2} = 0.25 \times 10^{-3} \text{ W sr}^{-1} \text{m}^{-2}$.

640

641 **Figure 3** depicts the keogram of 630 nm airglow images (as observed in the Figure 1 on 15
 642 August 2017) averaged in 50 bins in the North-South direction and their time evolution (x axes)
 643 is shown for the West (bottom) to East (top) direction in single pixel levels. The pixels are
 644 converted into rectilinear geographical coordinates for the height of 250 km centred over KU,
 645 Srinagar.

646

647 **Figure 4** shows the same as the Figure 3 except that North-South and East-West are
 648 interchanged in the present keogram.

649

650 **Figure 5** illustrates the same as the Figure 3 but for the 840 nm emissions of OH molecules
 651 from the height of about 86 km (maximum zenith angle covered is $-57^\circ - 57^\circ$). The colorbar
 652 values (emission intensity) are given in $\text{W sr}^{-1} \text{m}^{-2}$ which can be converted into Rayleigh unit
 653 as $1 \text{ Rayleigh} = 10^{-9}/2\pi\lambda \text{ W sr}^{-1} \text{m}^{-2} = 10^{-3}/2\pi \cdot 0.84 \text{ W sr}^{-1} \text{m}^{-2} = 0.19 \times 10^{-3} \text{ W sr}^{-1} \text{m}^{-2}$.

654

655

656 **Figure 6** illustrates the same as the Figure 4 but for the 840 nm emissions of OH molecules
 657 from the height of about 86 km.

658 **Figure 7** illustrates the same as the Figure 5 but for the 557.7nm emissions of atomic oxygen
 659 from the height of about 97 km. The colorbar values (emission intensity) are given in W sr^{-1}
 660 m^{-2} which can be converted into Rayleigh unit as $1 \text{ Rayleigh} = 10^{-9}/2\pi\lambda \text{ W sr}^{-1} \text{m}^{-2} = 10^{-3}/2\pi \cdot 0.557 \text{ W sr}^{-1} \text{m}^{-2} = 0.29 \times 10^{-3} \text{ W sr}^{-1} \text{m}^{-2}$.

662

663

664 **Figure 8** illustrates the same as the Figure 6 but for the 557.7nm emissions of atomic oxygen
665 from the height of about 97 km.

666

667 **Figure 9** provides the height profiles of wind speeds (TIDI-TIMED satellite data) obtained for
668 few longitudes and latitudes centred around the Kashmir region

669

670 **Figure 10** depicts the ECMWF reanalyses 5 (ERA-5) zonal and meridional wind velocities at
671 700 mb and 500 mb levels at 15:00 UT on 15 August 2017

672

673 **Figure 11** shows the topographic (ISRO-Bhuvan data) structure of the erstwhile state of Jammu
674 and Kashmir (J&K), India corresponding to the Figure 10. The imager station, Srinagar,
675 marked as asterisk symbol, is located in the present J&K Union Territory of India.

676

677 **Figure 12** presents the results of SAMI3 ionosphere model (a) time evolution (13:30 – 24:00
678 UT) of electron density in the heights of 85-150 km for the Srinagar location (75E; 34N
679 geographic) on 15 August 2017 (b) same as a except for the heights of 85-500 km and time of
680 00:00-24:00 UT.

681

682 **Figure 13** Illustrates the contour plots (x and y axes for latitude and longitude respectively) of
683 electron density (SAMI3 model) at the height of 125 km centred over the CCD imager location
684 of Srinagar, at (a) 13:30 UT (b) 14:00 UT (c) 14:30 UT (d) 15:00 UT (e) 15:30 UT (f) 16:00
685 UT (g) 16:30 UT and (h) 19:00 UT

686

687

688

689 **References:**

690

691

692 Afraimovich, E. L., N. P. Perevalova, and S. V. Voyeikov (2003), Traveling wave packets of
693 total electron content disturbances as deduced from global GPS network data, *J. Atmos. Sol.*
694 *Terr. Phys.*, 65(11), 1245–1262.

695

696 Alok, Taori, A., A. Jayaraman, V. Kamalakar, Imaging of mesosphere–thermosphere airglow
697 emissions over Gadanki (13.51N, 79.21E), (2013), — First results *Journal of Atmospheric and*
698 *Solar-Terrestrial Physics* 93 (2013) 21–28; <http://dx.doi.org/10.1016/j.jastp.2012.11.007>.

699

700 Bacmeister, J. Y., and M. R. Schoeberl, (1989) Break down of vertically propagating two-
701 dimensional gravity waves forced by orography, *J. of the Atmos. Sciences*, V46, No. 14, 1989.

702

703 Baker, D. J., and G. J. Romick (1976), The rayleigh: interpretation of the unit in terms of
704 column emission rate or apparent radiance expressed in SI units, *Applied Optics*, 15(8), 1976..

705

706 Durran, D. R., (1990), Mountain waves and downslope winds, *Atmospheric Processes Over*
707 *Complex Terrain*, Meteorological Monographs, **23** (45), University of Washington, American
708 Meteorological Society.

709

710 Dymond, K. F., C. Watts, C. Coker, S. A. Budzien, P. A. Bernhardt, N. Kassim, T. J. Lazio, K.
711 Weiler, P. C. Crane, P. S. Ray, A. Cohen, T. Clarke, L. J. Rickard, G. B. Taylor, F. Schinzel,
712 Y. Pihlstrom, M. Kuniyoshi, S. Close, P. Colestock, S. Myers, and A. Datta, (2011), A medium-

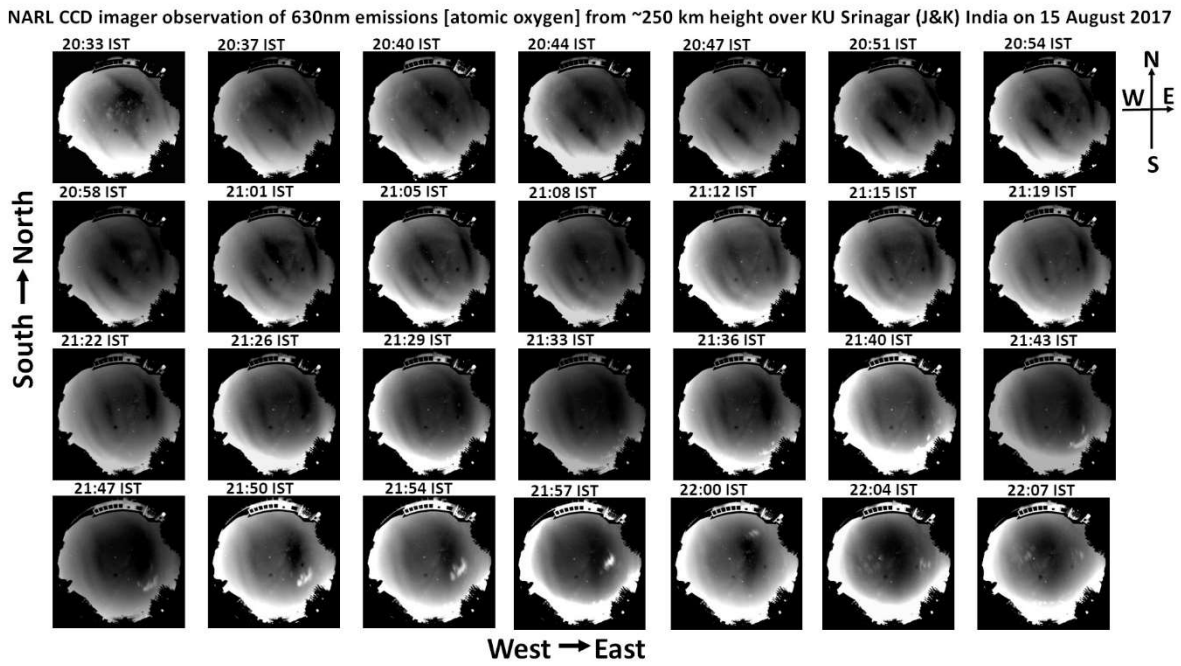
- 713 scale traveling ionospheric disturbance observed from the ground and from space, *Radio Sci.*,
 714 46, RS5010, doi:10.1029/2010RS004535.
- 715
- 716 F. J. Garcia, M. J. Taylor, and M. C. Kelley, (1997), Two-dimensional spectral analysis of
 717 mesospheric airglow image data, *APPLIED OPTICS* y Vol. 36, No. 29.
- 718
- 719 Figueiredo, C. A. O. B., Takahashi, H., Wrasse, C. M., Otsuka, Y., Shiokawa, K., and Barros,
 720 D. (2018). Medium-scale traveling ionospheric disturbances observed by detrended total
 721 electron content maps over Brazil. *Journal of Geophysical Research: Space Physics*, 123,
 722 2215–2227. <https://doi.org/10.1002/2017JA025021>
- 723 Francis, S. H. (1974), A theory of medium-scale traveling ionospheric disturbances, *Journal of*
 724 *Geophysical Research: Space Physics*, 79 (34).
- 725
- 726 Garcia, F. J., M. C. Kelley, J. J. Makela, and C.-S. Huang (2000), Airglow observations of
 727 mesoscale low-velocity traveling ionospheric disturbances at midlatitudes, *J. Geophys. Res.*,
 728 105, 18,407 – 18,415, doi:10.1029/1999JA000305.
- 729
- 730 Guanyi Chen, Chen Zhou , Yi Liu, Jiaqi Zhao, Qiong Tang, Xiang Wang and Zhengyu Zhao,
 731 (2019) A statistical analysis of medium-scale traveling ionospheric disturbances during 2014–
 732 2017 using the Hong Kong CORS network *Earth, Planets and space*,
 733 <https://doi.org/10.1186/s40623-019-1031-9>
- 734
- 735 Herna'ndez-Pajares, M., J.M. Juan, and J. Sanz (2006), Medium-scale traveling ionospheric
 736 disturbances affecting GPS measurements: Spatial and temporal analysis, *J. Geophys. Res.*,
 737 111, A07S11, doi:10.1029/2005JA011474.
- 738
- 739 Hernández-Pajares, M., J. M. Juan, J. Sanz, and A. Aragón-Àngel (2012), Propagation of
 740 medium scale traveling ionospheric disturbances at different latitudes and solar cycle
 741 conditions, *Radio Sci.*, 47, RS0K05, doi:10.1029/2011RS004951
- 742
- 743 Hines, C. O. (1972), *The Upper Atmosphere in Motion*, Heffernan, Worcester, Mass.
- 744
- 745 Hines, C. O. (1974), *The upper atmosphere in motion*, American Geophysical Union,
 746 Washington D. C. *J. Geophys. Res.*, 79, 5245–5260.
- 747
- 748 Hines, C. O., (1960) Internal atmospheric gravity waves at ionospheric heights, *Can. J. Phys.*,
 749 38, 1441–1481.
- 750
- 751 Hocke, K., and Schlegel, K. (1996), A review of atmospheric gravity waves and travelling
 752 ionospheric disturbances: 1982-1995, *Ann. Geophysicae*, 14, 917-940.
- 753
- 754 Huba, J. D, and J. Krall (2013), Modeling the plasmasphere with SAMI3, *Geophys. Res. Lett.*,
 755 40, 6–10, doi:10.1029/2012GL054300, 20131.
- 756
- 757 Huba, J. D., G. Joyce, and J. A. Fedder (2000), SAMI2 (SAMI2 is another model of the
 758 ionosphere): A new low-latitude ionosphere model. *J. Geophys. Res.*, 105, 23,035.
- 759
- 760 Huba, J. D., G. Joyce, and J. Krall (2008), Three-dimensional equatorial spread F modeling,
 761 *Geophys. Res. Lett.*, 35, L10102, doi:10.1029/2008GL033509.
- 762

- 763 Hunsucker, R. D. (1982), Atmospheric gravity waves generated in the high latitude ionosphere:
764 A review, *Rev. Geophys.*, 20, 293–315, doi:10.1029/RG020i002p00293.
765
- 766 Jacobson, A. R., and W. C. Erickson (1992a), A method for characterizing transient
767 ionospheric disturbances using a large radiotelescope array, *Astron. Astrophys.*, 257, 401–409.
768
- 769 Jacobson, A. R., and W. C. Erickson (1992b), Wavenumber-resolved observations of
770 ionospheric waves using the Very Large Array radio telescope, *Planet. Space Sci.*, 40, 447–
771 455, doi:10.1016/0032-0633(92)90163-I.
- 772 Jacobson, A. R., R. C. Carlos, R. S. Massey, and G. Wu (1995), Observations of traveling
773 ionospheric disturbances with a satellite-beacon radio interferometer: Seasonal and local time
774 behavior, *J. Geophys. Res.*, 100, 1653–1665, doi:10.1029/94JA02663.
775
- 776 Jonah, O. F., Kherani, E. A., De Paula, E. R., (2016), Observation of TEC perturbation
777 associated with medium-scale traveling ionospheric disturbance and possible seeding
778 mechanism of atmospheric gravity wave at a Brazilian sector. *Journal of Geophysical*
779 *Research*, v. 121, n. 3, p. s 2531–2546, 2016. doi:10.1002/2015JA022273, 2016.
780
- 781 Kelley, M. C. and C. A. Miller, (1997), Electrodynamics of mid latitude spread F, 3.
782 Electrohydrodynamic waves? A new look at the role of electric fields in thermospheric wave
783 dynamics, *J. Geophys. Res.*, 102, 11,539–11,547, 1997.
784
- 785 Killeen, T. L., Wilbert R. Skinner, Roberta M. Johnson, Charles J. Edmonson, Qian Wu, Rick
786 J. Niciejewski, Heinz J. Grassl, David A. Gell, Peter E. Hansen, Jon D. Harvey, and Julie F.
787 Kafkalidis, (1999), TIMED Doppler Interferometer (TIDI), 1-13, SPIE99.
- 788 Kotake, N., Y. Otsuka, T. Ogawa, T. Tsugawa, and A. Saito (2007), Statistical study of
789 medium-scale traveling ionospheric disturbances observed with the GPS networks in southern
790 California, *Earth Planets Space*, 59, 95–102.
791
- 792 Kotake, N., Y. Otsuka, T. Ogawa, T. Tsugawa, and A. Saito (2007), Statistical study of
793 medium-scale traveling ionospheric disturbances observed with the GPS networks in Southern
794 California, *Earth Planets Space*, 59, 95– 102.
795
- 796 Kotake, N., Y. Otsuka, T. Tsugawa, T. Ogawa, and A. Saito (2006), Climatological study of
797 GPS total electron content variations caused by medium-scale traveling ionospheric
798 disturbances, *J. Geophys. Res.*, 111, A04306, doi:10.1029/2005JA011418.
799
- 800 Kubota, M., Fukunishi, H., Okano, S., (2001), Characteristics of medium- and large-scale TIDs
801 over Japan derived from OI630nm night glow observation. *Earth Planets Space*, 53,741–751.
802
- 803 Kubota, M., K. Shiokawa, M. K. Ejiri, Y. Otsuka, T. Ogawa, T. Sakanoi, H. Fukunishi, M.
804 Yamamoto, S. Fukao, and A. Saito (2000), Traveling ionospheric disturbances observed in the
805 OI 630-nm nightglow images over Japan by using a multipoint imager network during the
806 FRONT campaign, *Geophys. Res. Lett.*, 27(24), 4037 – 4040, doi:10.1029/2000GL011858.
807
- 808 Lee, C. C., Y. A. Liou, Y. Otsuka, F. D. Chu, T. K. Yeh, K. Hoshino, and K. Matunaga (2008),
809 Nighttime medium-scale traveling ionospheric disturbances detected by network GPS
810 receivers in Taiwan, *J. Geophys. Res.*, 113, A12316, doi:10.1029/2008JA013250.

- 811
812 Liu, C. H., and K. C. Yeh (1969), Effect of ion drag on propagation of acoustic-gravity waves
813 in the atmospheric F region, *J. Geophys. Res.*, 74, 2248–2255, doi:10.1029/JA074i009p02248.
814
- 815 Liu, H.-L., and S. L. Vadas (2013), Large-scale ionospheric disturbances due to the dissipation
816 of convectively-generated gravity waves over Brazil, *J. Geophys. Res. Space Physics*, 118,
817 2419–2427, doi:10.1002/jgra.50244.
- 818 Mendillo, M., J. Baumgardner, D. Nottingham, J. Aarons, B. Reinisch, J. Scali, and M. Kelley,
819 Investigations of thermospheric-ionospheric dynamics with 6300°A images from the Arecibo
820 Observatory, *J. Geophys. Res.*, 102, 7331–7343, 1997.
821
- 822 Miller, C. A., W. E. Swartz, M. C. Kelley, M. Mendillo, D. Nottingham, J. Scali, and B.
823 Reinisch (1997), Electrodynamics of midlatitude spread F 1. Observations of unstable, gravity
824 wave-induced ionospheric electric fields at tropical latitudes, *J. Geophys. Res.*, 102, 11,521–
825 11,532, 1997.
826
- 827 Ogawa, T., N. Balan, Y. Otsuka, K. Shiokawa, C. Ihara, T. Shimomai, and A. Saito (2002),
828 Observations and modeling of 630 nm airglow and total electron content associated with
829 traveling ionospheric disturbances over Shigaraki, Japan, *Earth Planets Space*, 54, 45–56.
830
- 831 Otsuka, Y., F. Onoma, K. Shiokawa, T. Ogawa, M. Yamamoto, and S. Fukao (2007),
832 Simultaneous observations of nighttime medium-scale traveling ionospheric disturbances and
833 E region field-aligned irregularities at midlatitude, *J. Geophys. Res.*, 112, A06317,
834 doi:10.1029/2005JA011548.
835
- 836 Otsuka, Y., K. Shiokawa, T. Ogawa, and P. Wilkinson (2004), Geomagnetic conjugate
837 observations of medium-scale traveling ionospheric disturbances at midlatitude using all-sky
838 airglow imagers, *Geophys. Res. Lett.*, 31, L15803, doi:10.1029/2004GL020262.
839
- 840 Perkins, F. (1973), Spread F and ionospheric currents, *J. Geophys. Res.*, 78, 218– 226,
841 doi:10.1029/JA078i001p00218.
842
- 843 Saito, A., et al. (2001), Traveling ionospheric disturbances detected in the FRONT campaign,
844 *Geophys. Res. Lett.*, 28, 689 – 692, doi:10.1029/2000GL011884.
845
- 846 Saito, A., N. Nishimura, M. Yamamoto, S. Fukao, T. Tsugawa, Y. Otsuka, S. Miyazaki, and
847 M. C. Kelley (2002), Observations of traveling ionospheric disturbances and 3-m scale
848 irregularities in the nighttime F region ionosphere with the MU radar and a GPS network, *Earth*
849 *Planets Space*, 54, 31– 44.
850
- 851 Sau, S., Narayanan, V. L., Gurubaran, S., & Emperumal, K. (2018). Study of wave signatures
852 observed in thermosphere airglow imaging over dip equatorial region. *Advanced space*
853 *research*, 62(7), 1762–1774. <https://doi.org/10.1016/j.asr.2018.06.039>
854
- 855 Schunk, R. W., and A. F. Nagy (2000), *Ionospheres: Physics, Plasma Physics, and Chemistry*,
856 pp. 274–275, Cambridge Univ. Press, New York.
857
- 858 Shiokawa, K., C. Ihara, Y. Otsuka, and T. Ogawa (2003a), Statistical study of nighttime
859 medium-scale traveling ionospheric disturbances using midlatitude airglow images, *J.*
860 *Geophys. Res.*, 108(A1), 1052, doi:10.1029/ 2002JA009491.

- 861
862 Shiokawa, K., et al. (2005), Geomagnetic conjugate observation of nighttime medium-scale
863 and large-scale traveling ionospheric disturbances: FRONT3 campaign, *J. Geophys. Res.*, 110,
864 A05303, doi:10.1029/2004JA010845.
- 865
866 Shiokawa, K., Y. Otsuka, C. Ihara, T. Ogawa, and F. J. Rich (2003b), Ground and satellite
867 observations of nighttime medium-scale traveling ionospheric disturbance at midlatitude, *J.*
868 *Geophys. Res.*, 108(A4), 1145, doi:10.1029/2002JA009639.
- 869
870 Shiokawa, K., Y. Otsuka, M. K. Ejiri, Y. Sahai, T. Kadota, C. Ihara, T. Ogawa, K. Igarashi, S.
871 Miyazaki, and A. Saito (2002), Imaging observations of the equatorward limit of midlatitude
872 traveling ionospheric disturbances, *Earth Planets Space*, 54, 57– 62.
- 873
874 Tsugawa, T., Y. Otsuka, A. J. Coster, and A. Saito (2007), Medium-scale traveling ionospheric
875 disturbances detected with dense and wide TEC maps over North America, *Geophys. Res.*
876 *Lett.*, 34, L22101, doi:10.1029/2007GL031663.
- 877
878 Tsugawa, T., Y. Otsuka, A. J. Coster, and A. Saito (2007), Medium-scale traveling ionospheric
879 disturbances detected with dense and wide TEC maps over North America, *Geophys. Res.*
880 *Lett.*, 34, L22101, doi:10.1029/2007GL031663.
- 881
- 882 Vadas, S. L. (2013), Compressible f-plane solutions to body forces, heatings, and coolings, and
883 application to the primary and secondary gravity waves generated by a deep convective plume,
884 *J. Geophys. Res. Space Physics*, 118, 2377–2397, doi:10.1002/jgra.50163.
- 885 Vadas, S. L., and G. Crowley (2010), Sources of the traveling ionospheric disturbances
886 observed by the ionospheric TIDBIT sounder near Wallops Island on October 30, 2007, *J.*
887 *Geophys. Res.*, 115, A07324, doi:10.1029/2009JA015053.
- 888 Vadas, S. L., and H.-L. Liu (2009), The generation of large-scale gravity waves and neutral
889 winds in the thermosphere from the dissipation of convectively-generated gravity waves, *J.*
890 *Geophys. Res.*, 114, A10310, doi:10.1029/2009JA014108.
- 891 Vadas, S. L., and H.-L. Liu (2013), Numerical modeling of the large-scale neutral and plasma
892 responses to the body forces created by the dissipation of gravity waves from 6 h of deep
893 convection in Brazil, *J. Geophys. Res. Space Physics*, 118, 2593–2617,
894 doi:10.1002/jgra.50249.
- 895
896
897
898
899
900

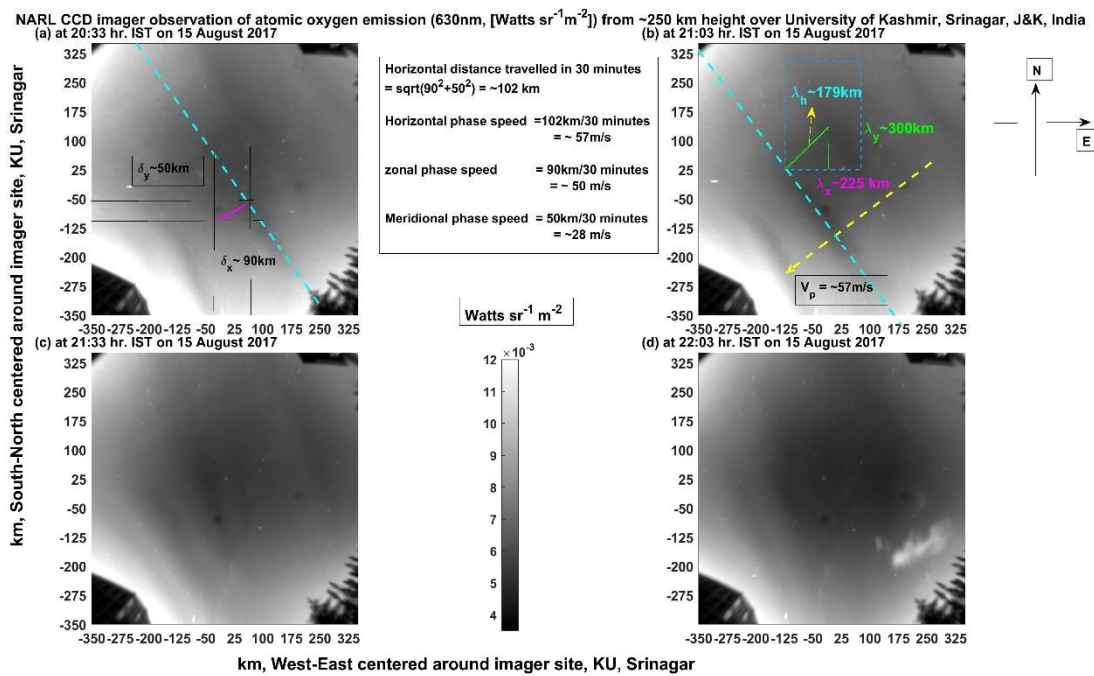
901 **Figure 1**



902

903 **Figure 2**

904

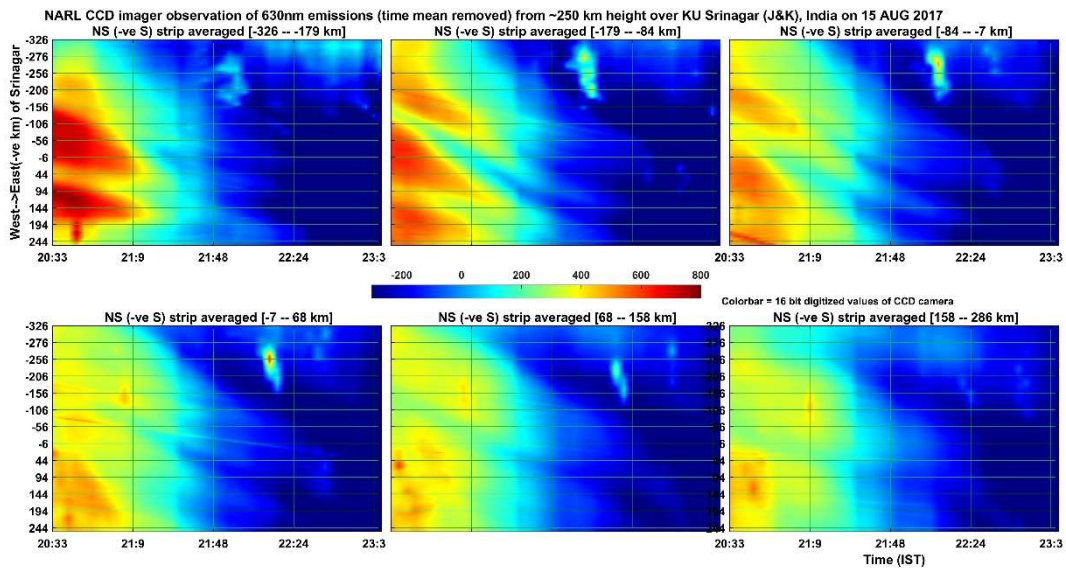


905

906

907 **Figure 3**

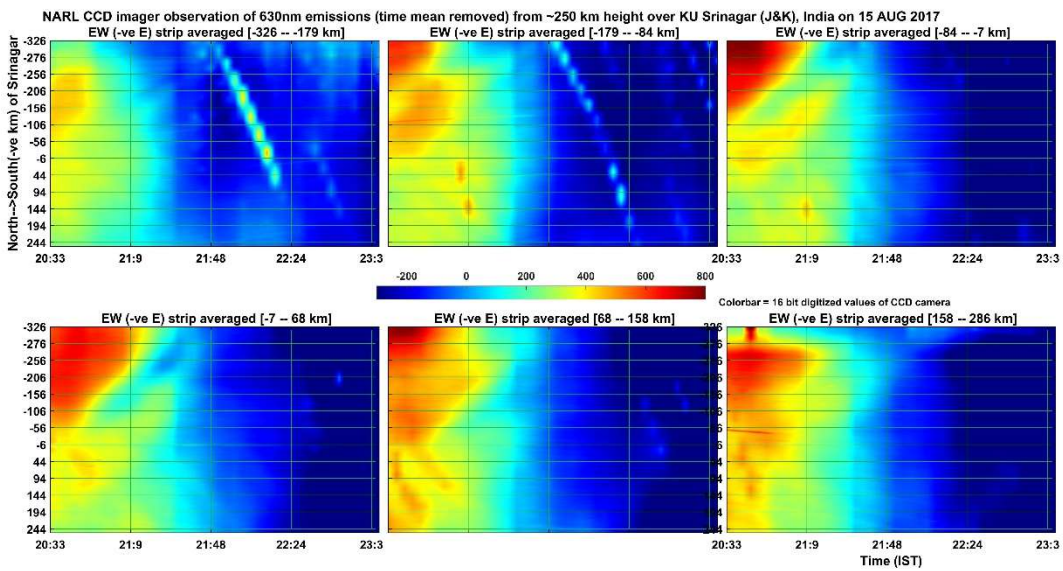
908



909

910 **Figure 4**

911



912

913

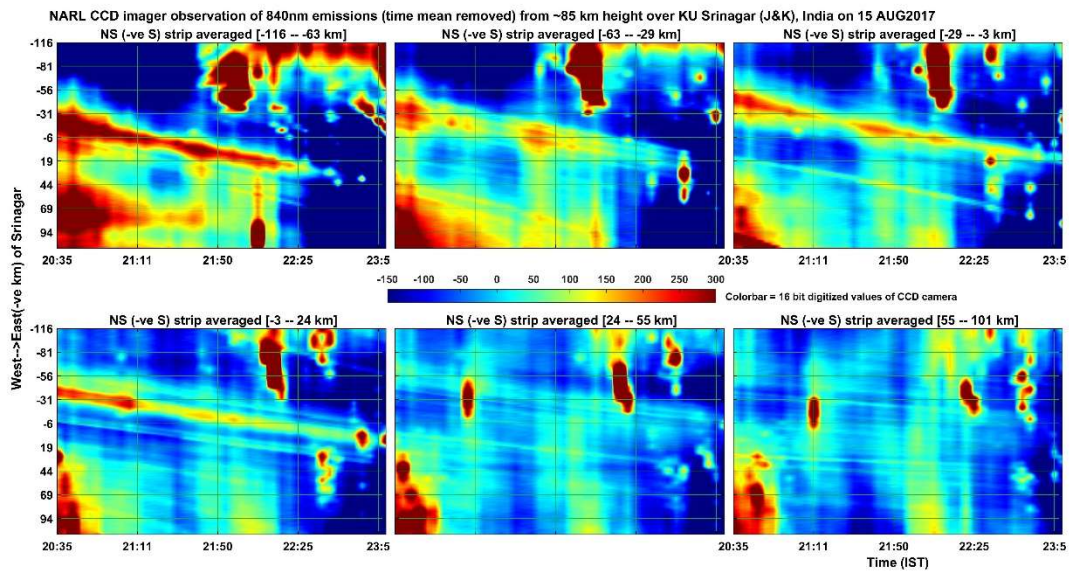
914

915

916

917 **Figure 5**

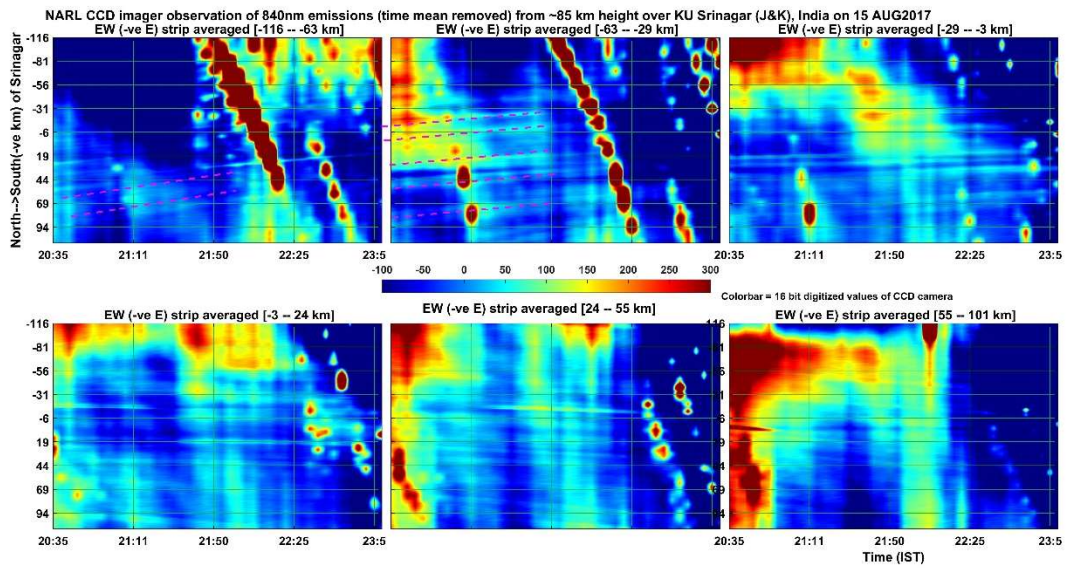
918



919

920 **Figure 6**

921



922

923

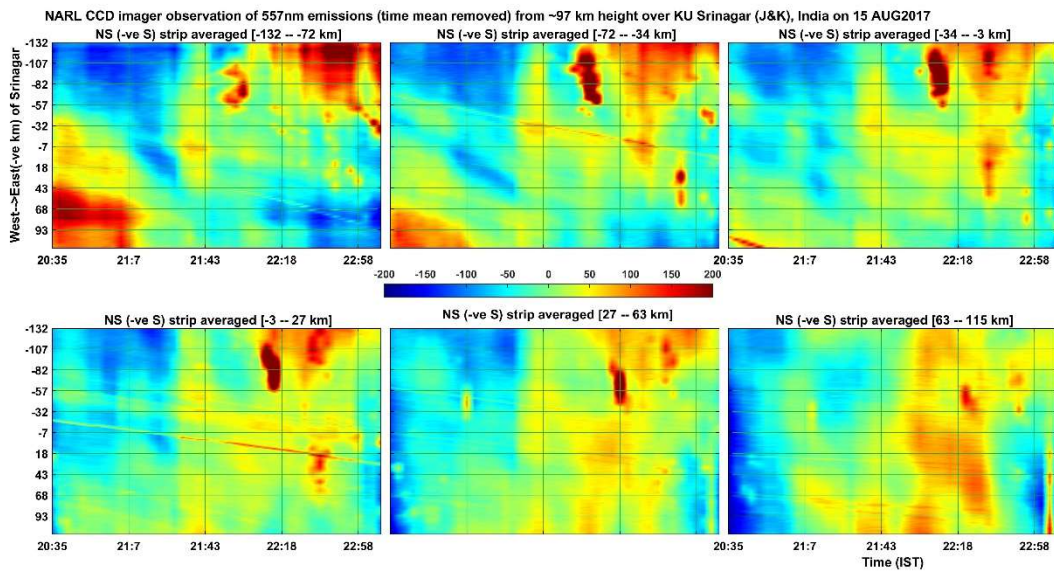
924

925

926

927 **Figure 7**

928

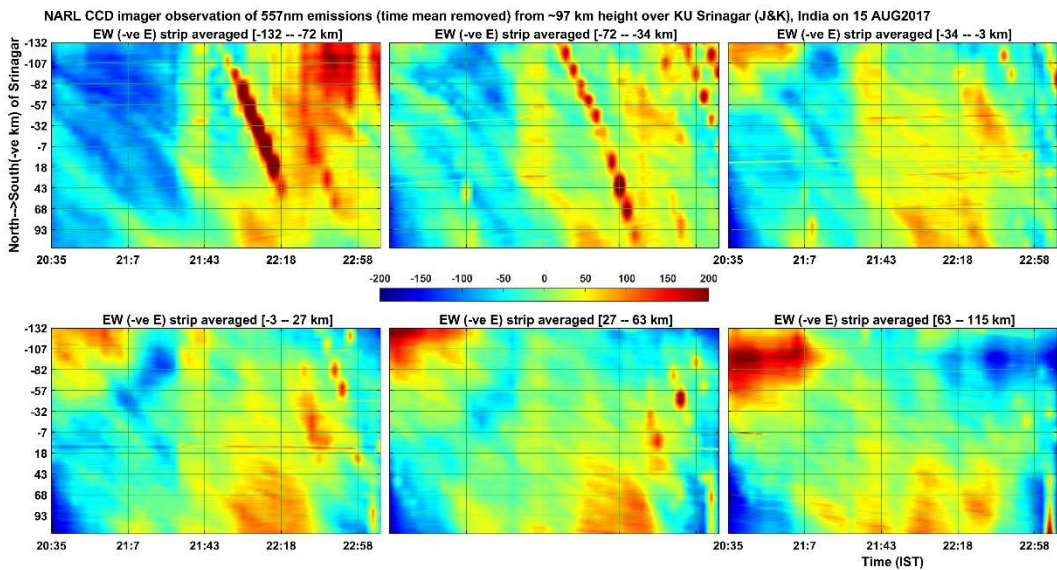


929

930

931 **Figure 8**

932



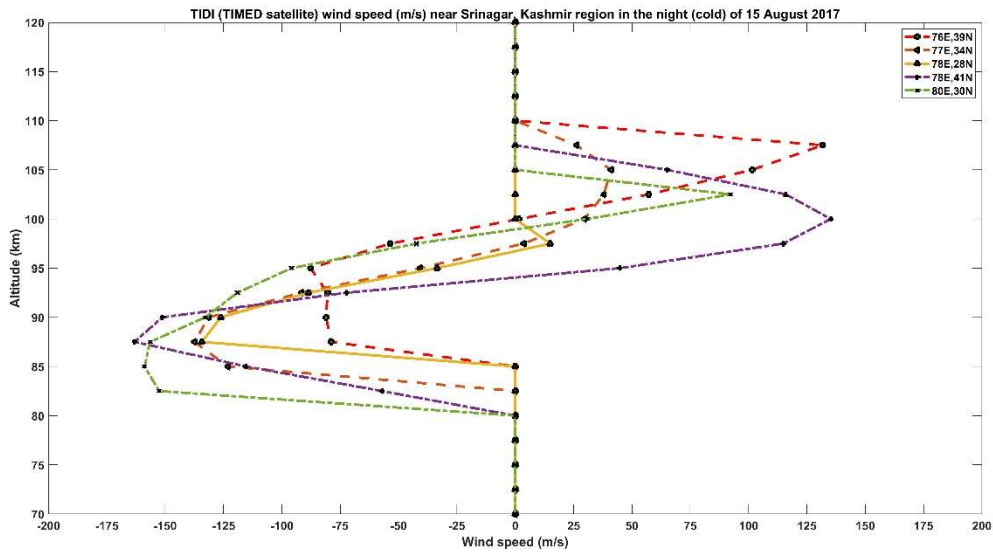
942

943

944

945 **Figure 9**

946

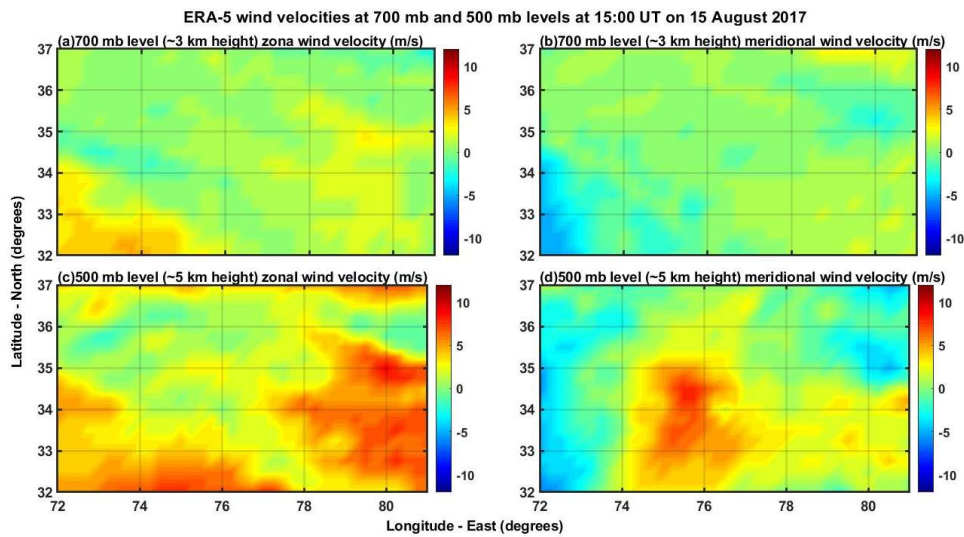


947

948

949 **Figure 10**

950



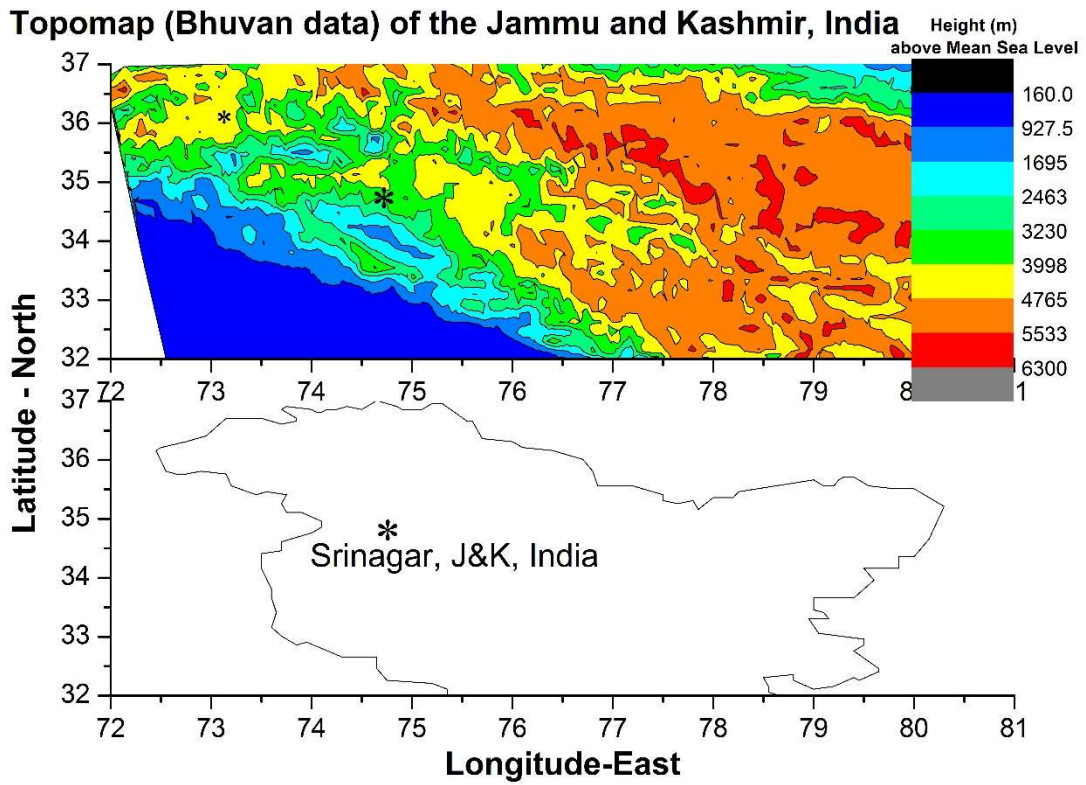
960

961

962

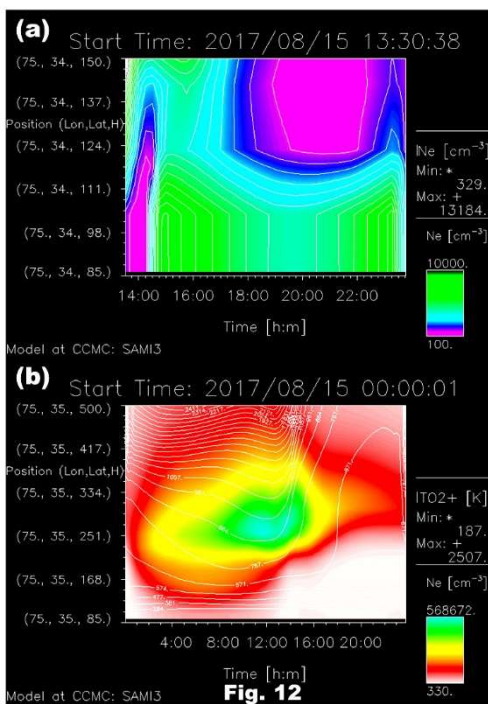
963

964 **Figure 11**



965

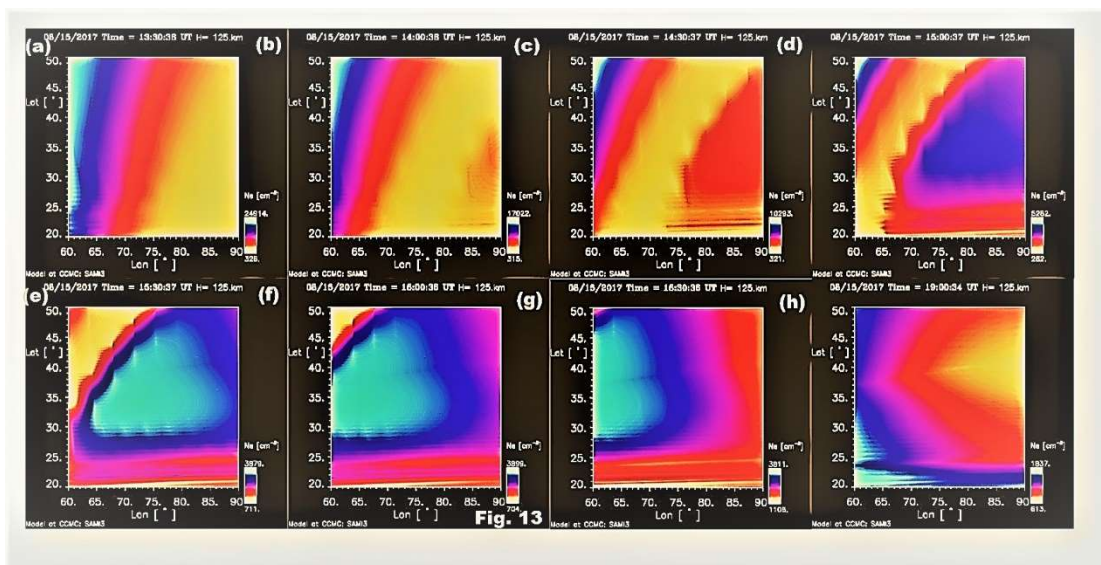
966 **Figure 12**



///

978 **Figure 13**

979



Figures

NARL CCD imager observation of 630nm emissions [atomic oxygen] from ~250 km height over KU Srinagar (J&K) India on 15 August 2017

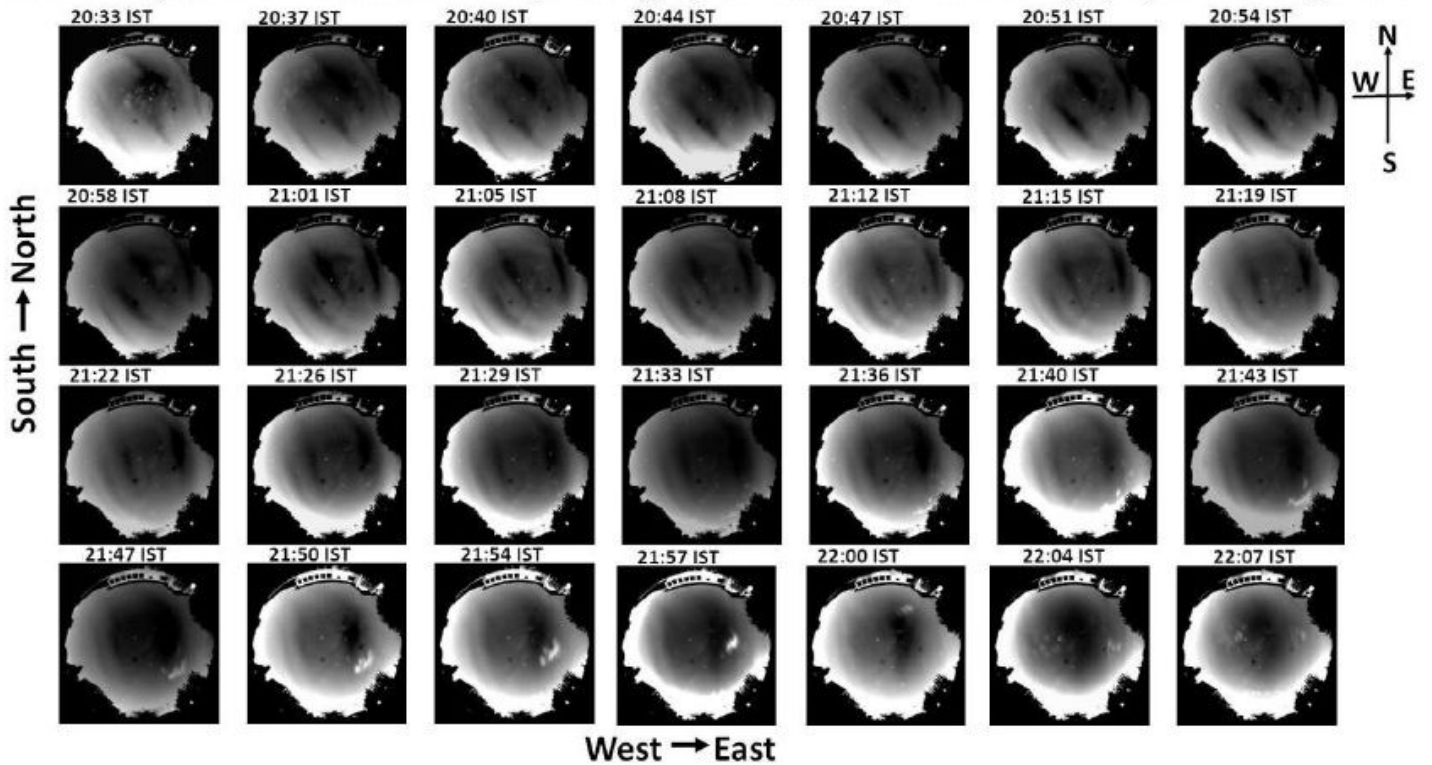


Figure 1

shows 36 panels (scans) of all-sky airglow images taken with NARL CCD imager at 630 nm (2nm band width) for atomic oxygen emissions at ~250 km height in the campus of University of Kashmir (KU), Srinagar, Jammu and Kashmir, India on 15 August 2017. The scan time is 100 seconds and the time interval of the scans is about 4 minutes.

NARL CCD imager observation of atomic oxygen emission (630nm, [$\text{Watts sr}^{-1} \text{m}^{-2}$]) from ~ 250 km height over University of Kashmir, Srinagar, J&K, India
 (a) at 20:33 hr. IST on 15 August 2017

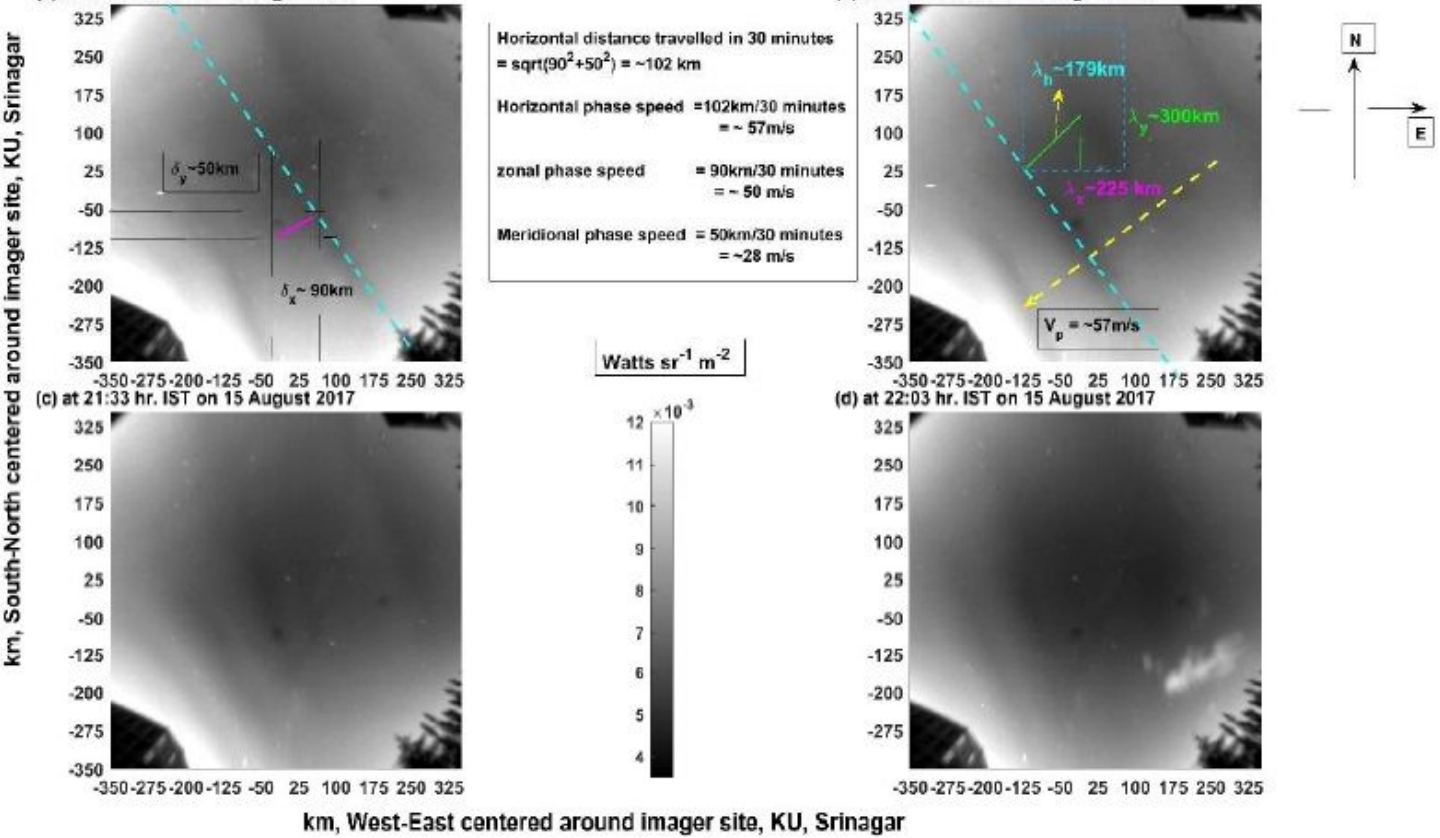


Figure 2

illustrates the rectilinear-geographical spatial information of 630 nm emissions as shown in Fig. 1 (on 15 August 2017) for four scans separated by half an hour. While the y axes (zenith angle of $-57^\circ - 57^\circ$) run from South (bottom) to North (top), the x axes (zenith angle of $-57^\circ - 57^\circ$) run from West (left) to East (right) centred over KU, Srinagar. The colour bar values (emission intensity) are given in $\text{W sr}^{-1} \text{m}^{-2}$ which can be converted into Rayleigh unit as $1 \text{ Rayleigh} = 10^{-9} / 2\pi\lambda \text{ W sr}^{-1} \text{m}^{-2} = 10^{-3} / 2\pi \cdot 0.63 \text{ W sr}^{-1} \text{m}^{-2} = 0.25 \times 10^{-3} \text{ W sr}^{-1} \text{m}^{-2}$.

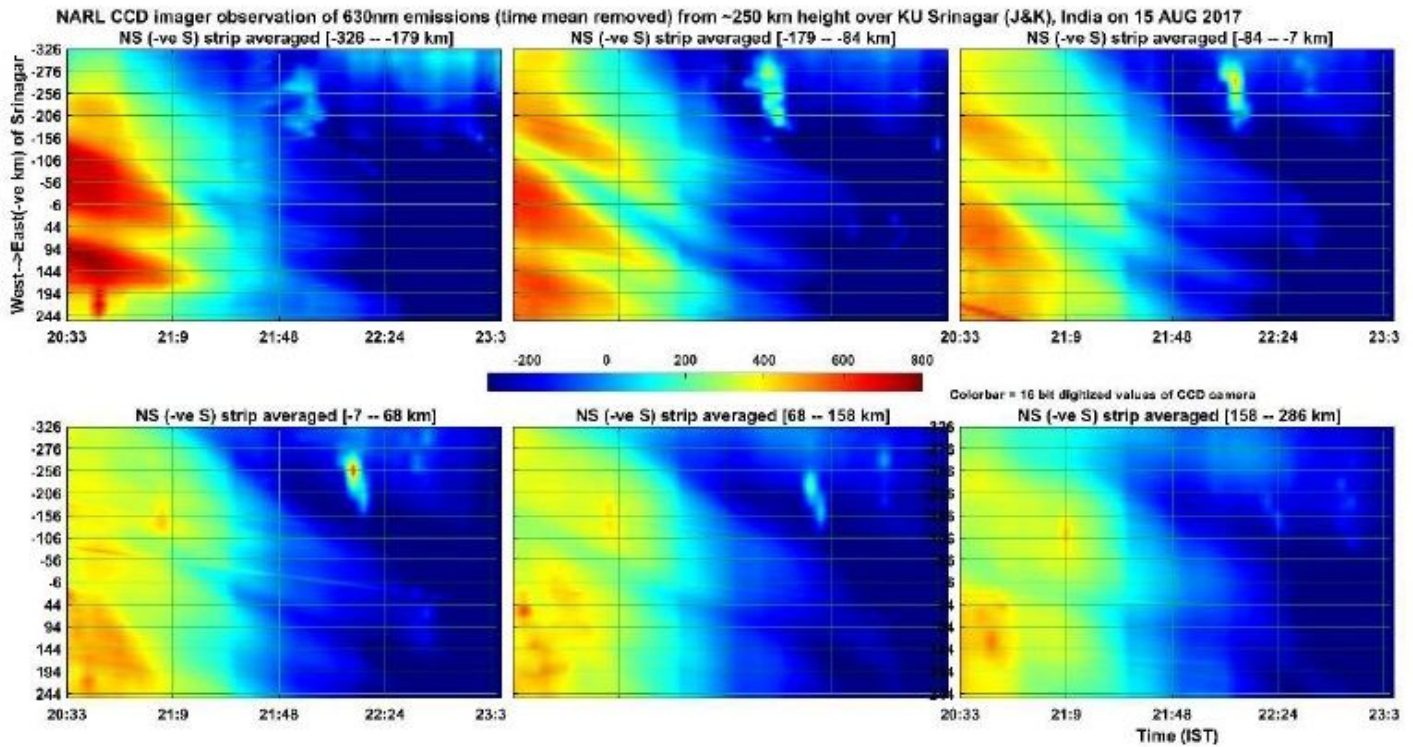


Figure 3

depicts the keogram of 630 nm airglow images (as observed in the Figure 1 on 15 August 2017) averaged in 50 bins in the North-South direction and their time evolution (x axes) is shown for the West (bottom) to East (top) direction in single pixel levels. The pixels are converted into rectilinear geographical coordinates for the height of 250 km centred over KU, Srinagar.

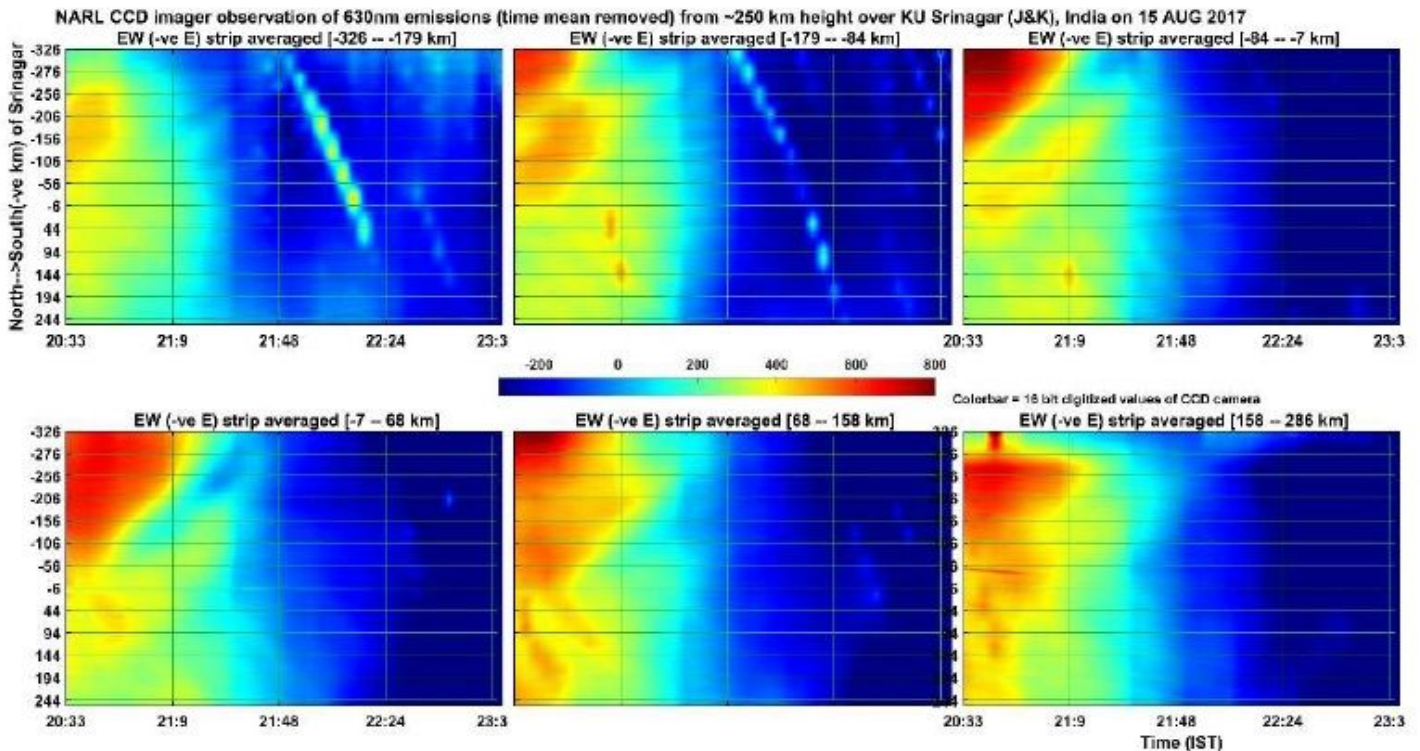


Figure 4

shows the same as the Figure 3 except that North-South and East-West are interchanged in the present keogram.

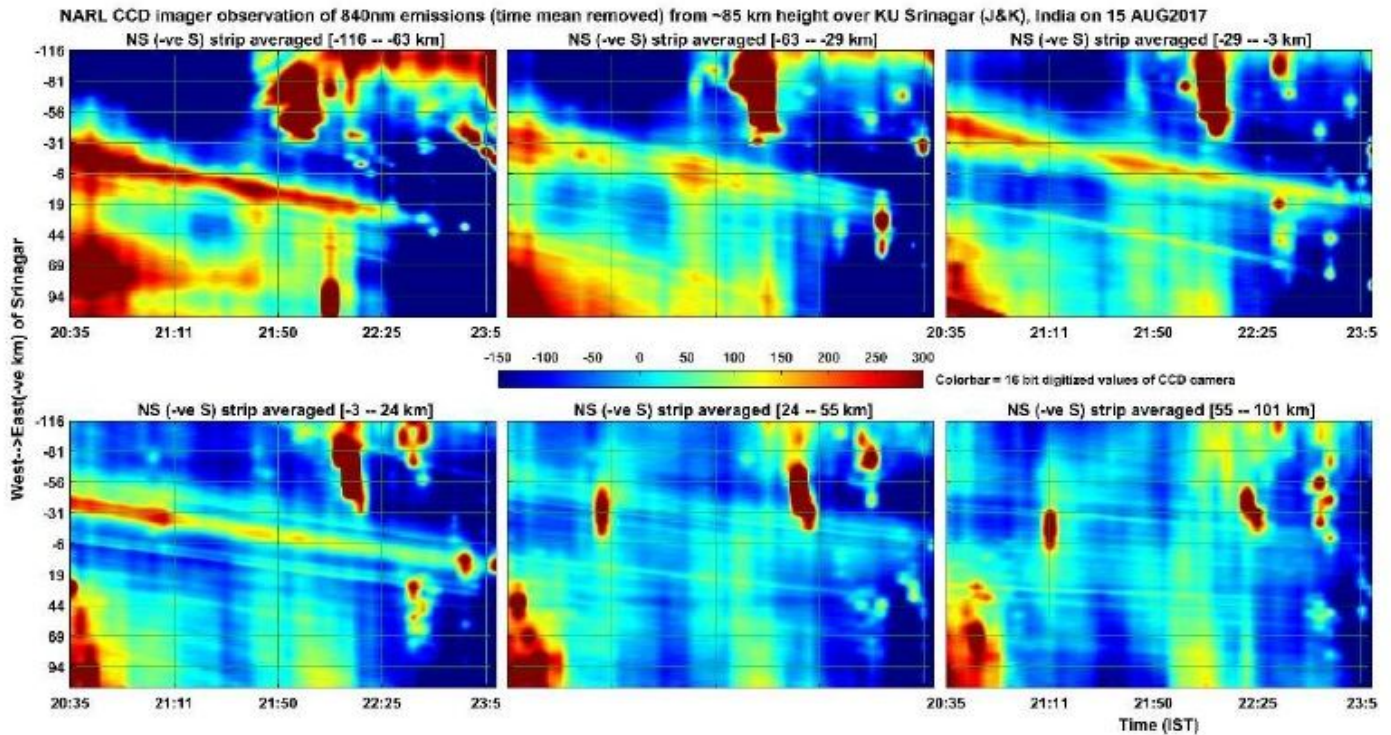


Figure 5

illustrates the same as the Figure 3 but for the 840 nm emissions of OH molecules from the height of about 86 km (maximum zenith angle covered is $-57^\circ - 57^\circ$). The colorbar values (emission intensity) are given in $\text{W sr}^{-1} \text{m}^{-2}$ which can be converted into Rayleigh unit as $1 \text{ Rayleigh} = 10^{-9}/2\pi\lambda \text{ W sr}^{-1} \text{m}^{-2} = 10^{-3}/2\pi \cdot 0.84 \text{ W sr}^{-1} \text{m}^{-2} = 0.19 \times 10^{-3} \text{ W sr}^{-1} \text{m}^{-2}$.

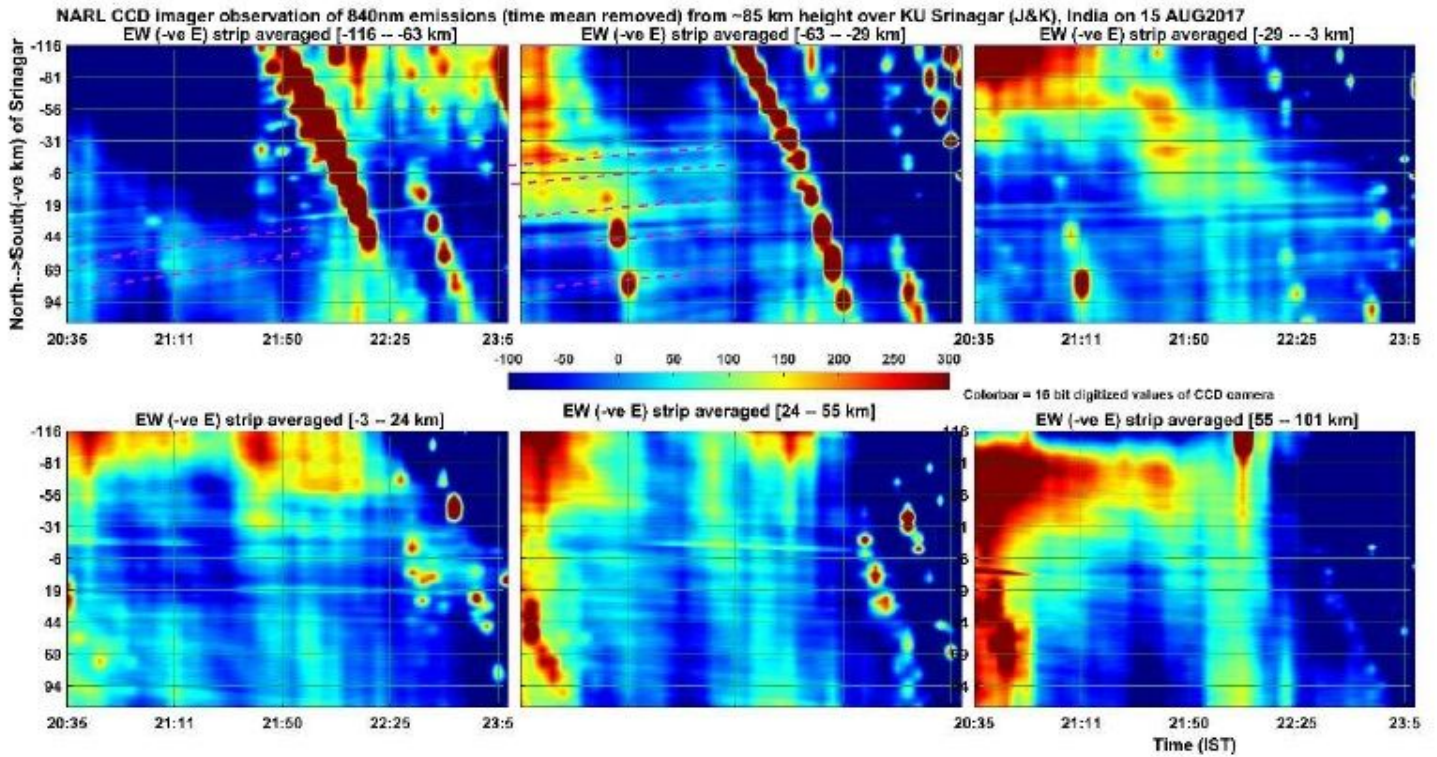


Figure 6

illustrates the same as the Figure 4 but for the 840 nm emissions of OH molecules from the height of about 86 km.

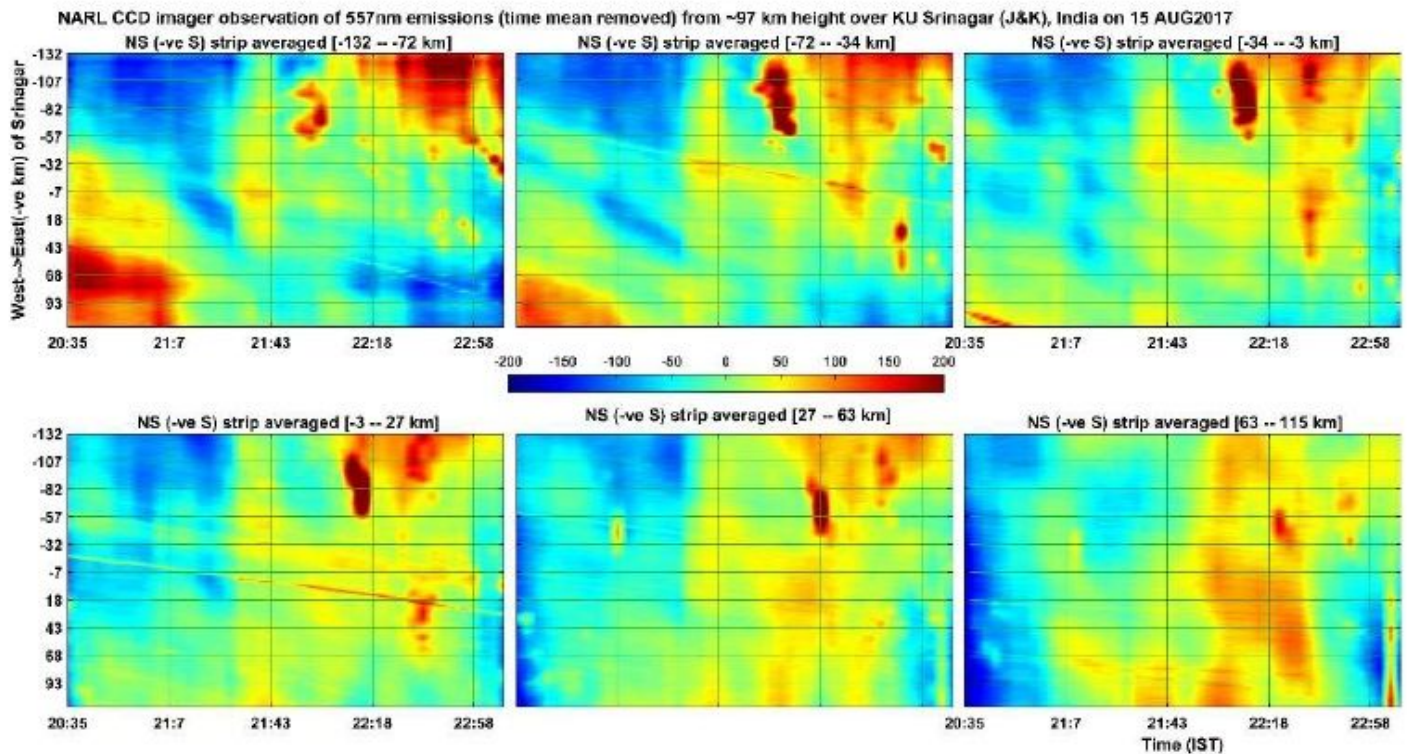


Figure 7

illustrates the same as the Figure 5 but for the 557.7nm emissions of atomic oxygen from the height of about 97 km. The colorbar values (emission intensity) are given in W sr-1 m-2 which can be converted into Rayleigh unit as $1 \text{ Rayleigh} = 10^{-9}/2\pi\lambda \text{ W sr}^{-1} \text{ m}^{-2} = 10^{-3}/2\pi \times 0.557 \text{ W sr}^{-1} \text{ m}^{-2} = 0.29 \times 10^{-3} \text{ W sr}^{-1} \text{ m}^{-2}$.

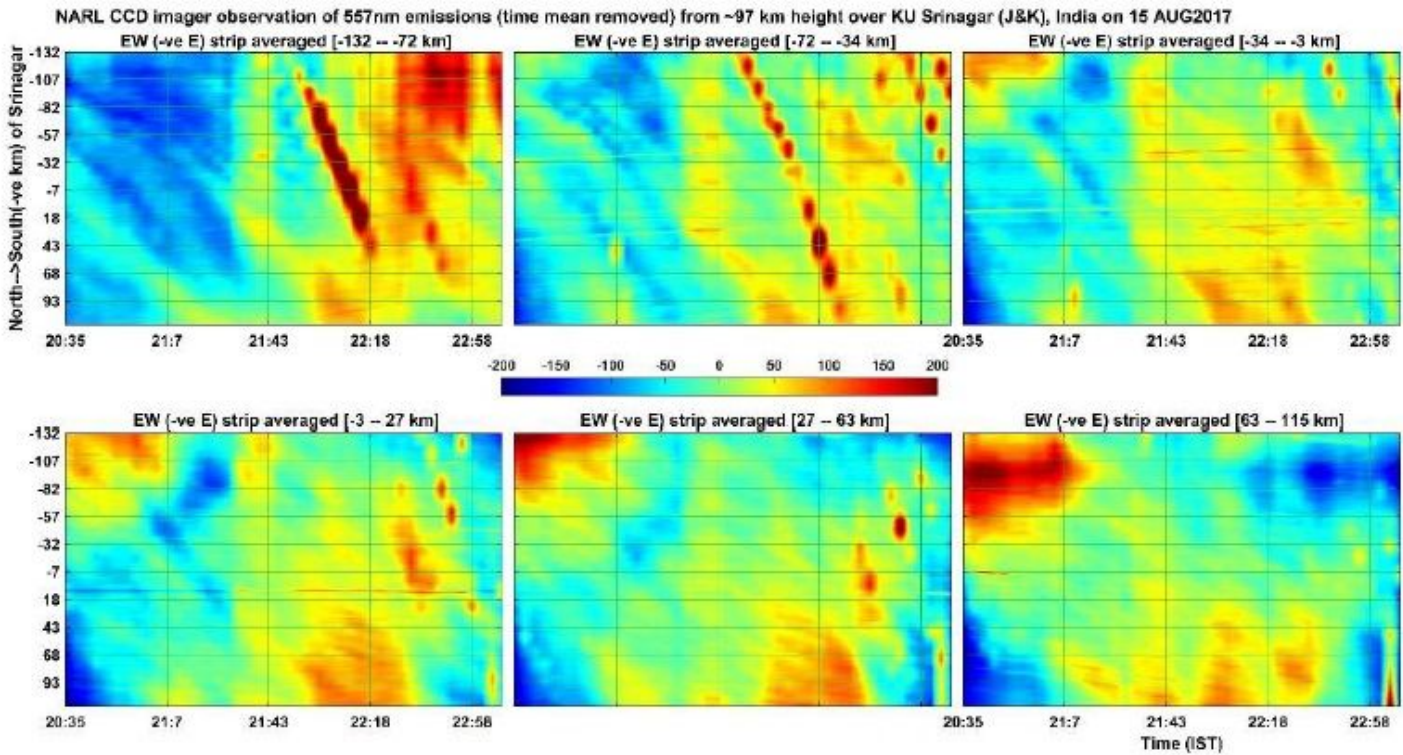


Figure 8

illustrates the same as the Figure 6 but for the 557.7nm emissions of atomic oxygen from the height of about 97 km.

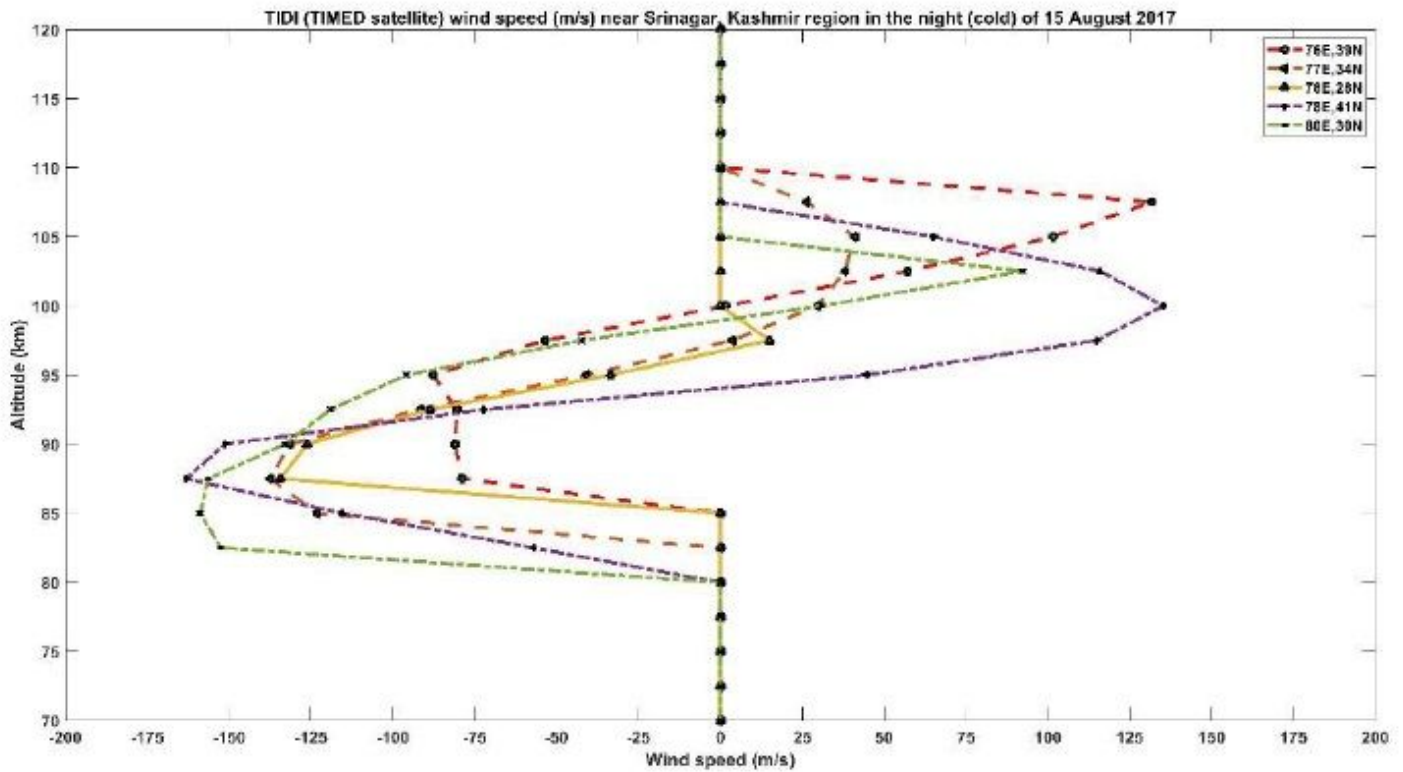


Figure 9

provides the height profiles of wind speeds (TIDI-TIMED satellite data) obtained for few longitudes and latitudes centred around the Kashmir region

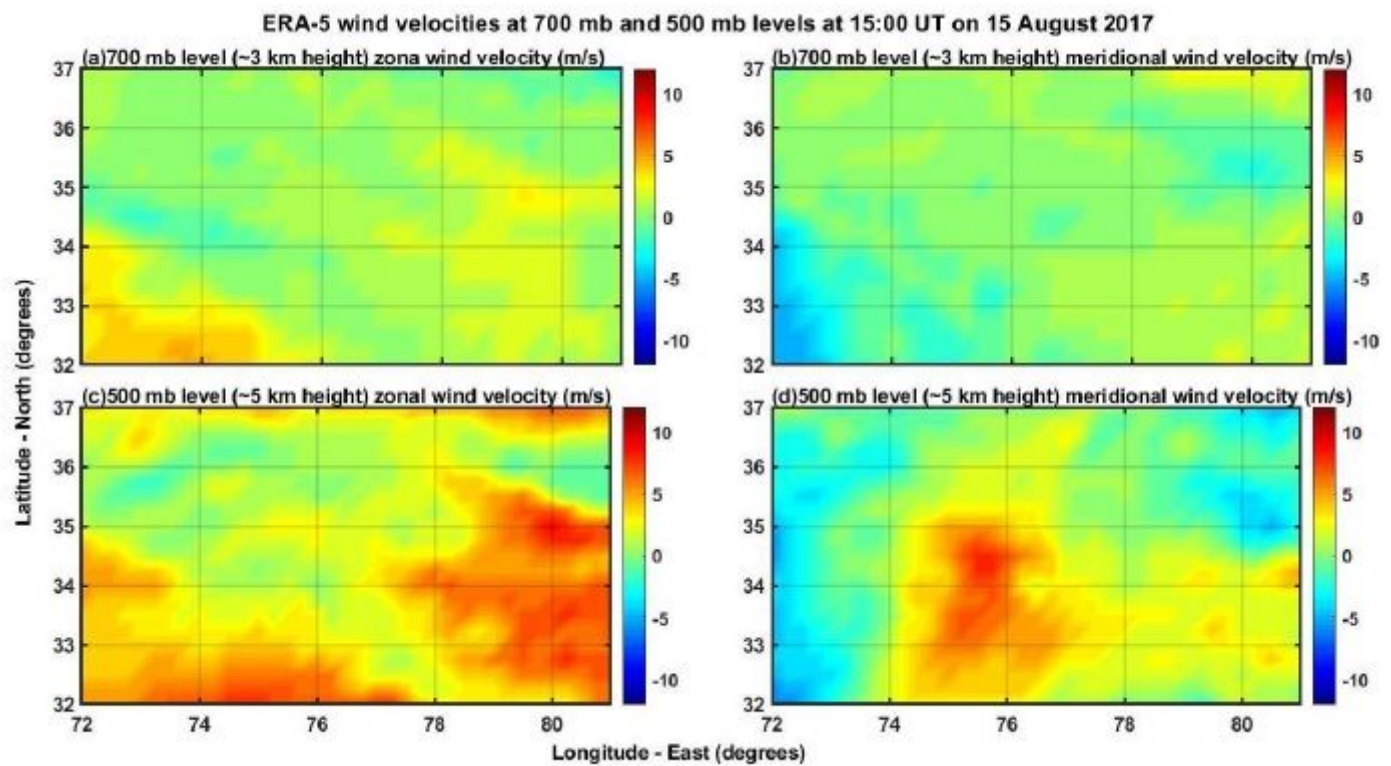


Figure 10

depicts the ECMWF reanalyses 5 (ERA-5) zonal and meridional wind velocities at 700 mb and 500 mb levels at 15:00 UT on 15 August 2017

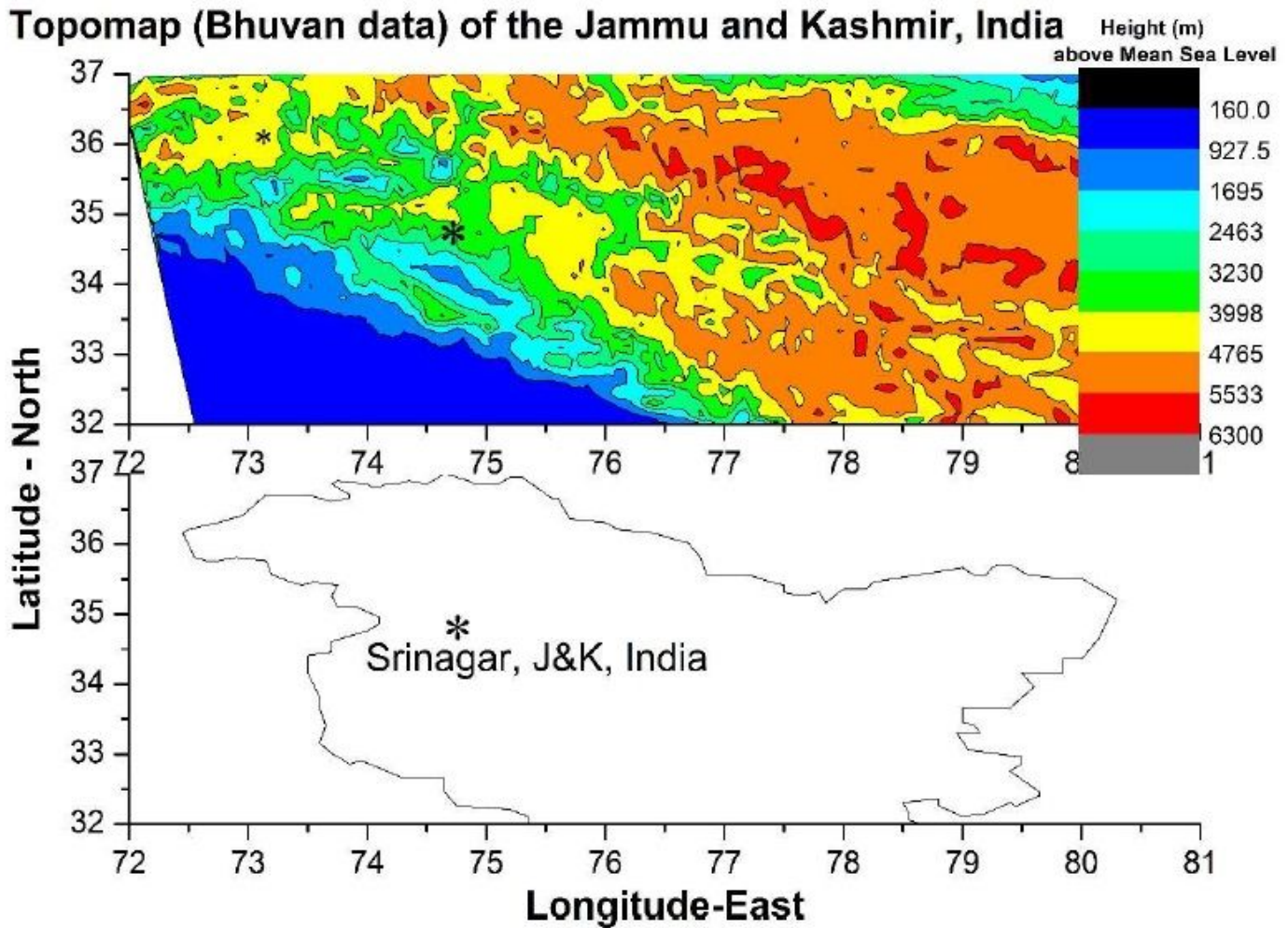


Figure 11

shows the topographic (ISRO-Bhuvan data) structure of the erstwhile state of Jammu and Kashmir (J&K), India corresponding to the Figure 10. The imager station, Srinagar, marked as asterisk symbol, is located in the present J&K Union Territory of India.

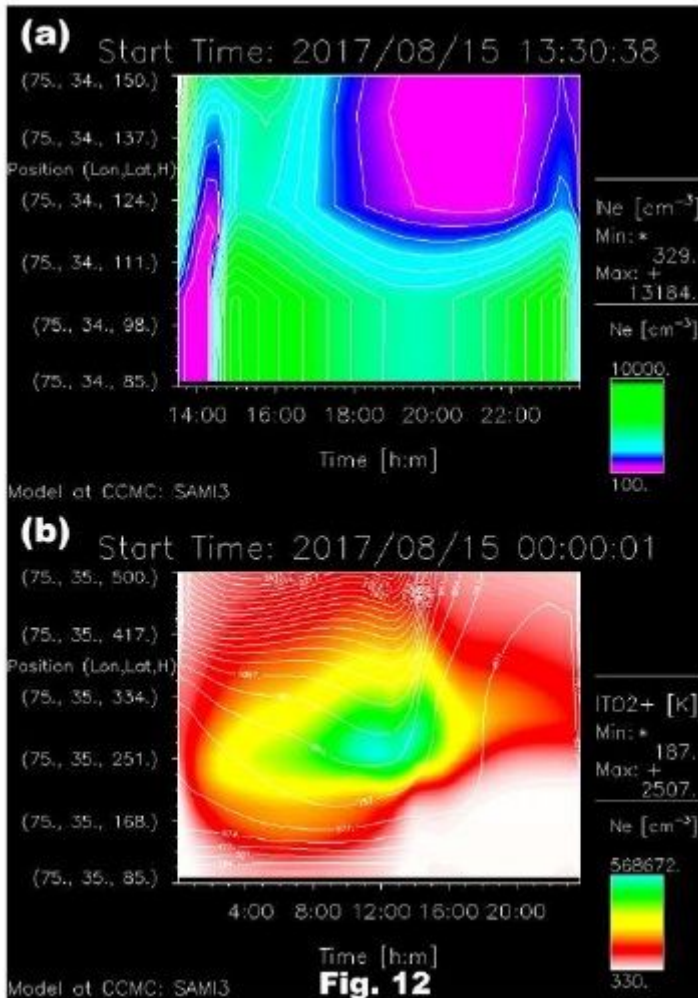


Figure 12

presents the results of SAMI3 ionosphere model (a) time evolution (13:30 – 24:00 UT) of electron density in the heights of 85-150 km for the Srinagar location (75E; 34N geographic) on 15 August 2017 (b) same as a except for the heights of 85-500 km and time of 00:00-24:00 UT.

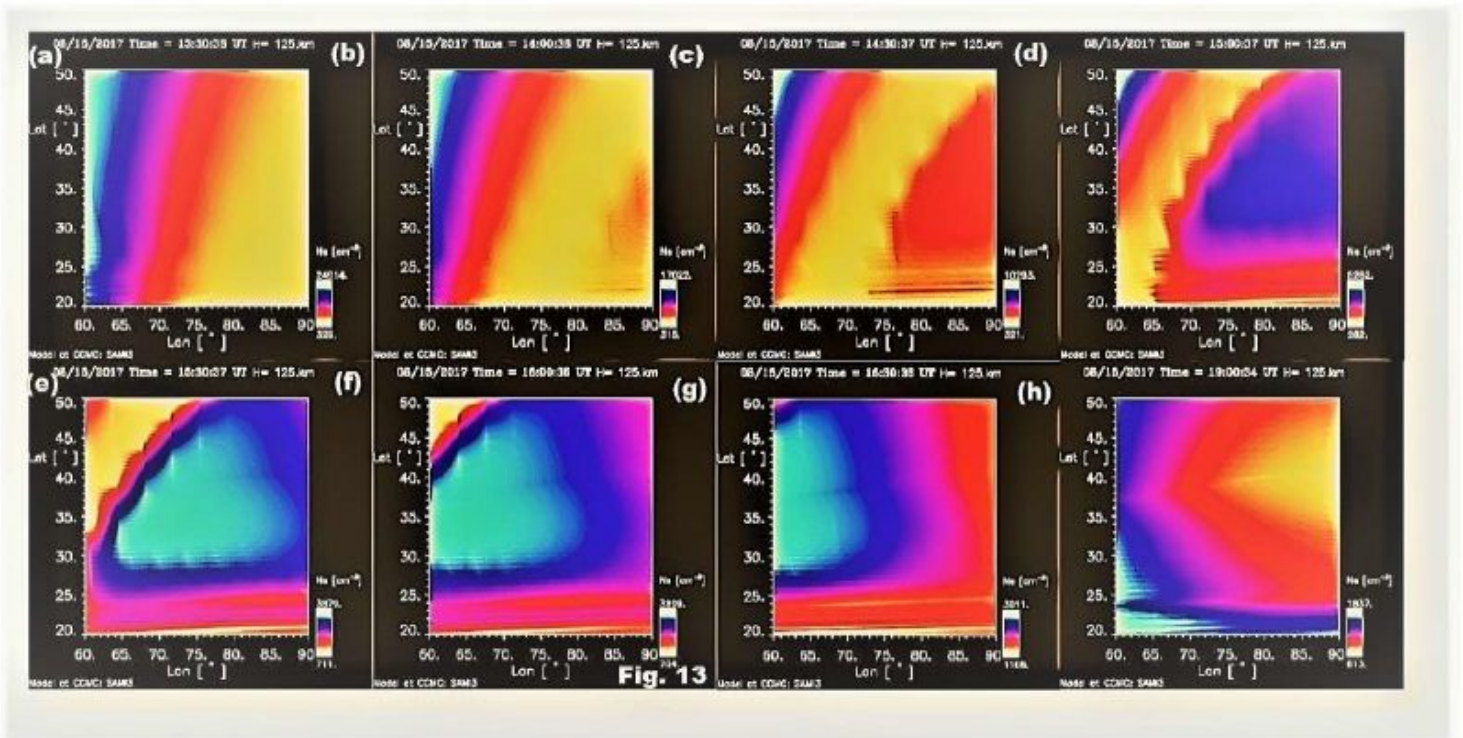


Figure 13

Illustrates the contour plots (x and y axes for latitude and longitude respectively) of electron density (SAMI3 model) at the height of 125 km centred over the CCD imager location of Srinagar, at (a) 13:30 UT (b) 14:00 UT (c) 14:30 UT (d) 15:00 UT (e) 15:30 UT (f) 16:00 UT (g) 16:30 UT and (h) 19:00 UT